



Modelling non-linear cyclic stress-strain behaviour of stainless steel reinforcing bars

H. Moodley^{a,*}, R. De Risi^b, S. Afshan^a

^a Faculty of Engineering and Physical Sciences, University of Southampton, UK

^b School of Civil, Aerospace and Design Engineering, University of Bristol, UK

ARTICLE INFO

Keywords:

Cyclic stress-strain modelling
Experimental testing
Fibre-section modelling
Inelastic buckling
OpenSees

ABSTRACT

This paper presents a newly calibrated set of uniaxial cyclic material parameters for stainless steel rebars, tailored for modelling reinforced concrete structures using the constitutive formulations *Steel02* and *Hysteretic* in OpenSees. The study provides new stress-strain data from 84 tests, including monotonic tension, compression and cyclic loading of stainless steel rebars, hot-rolled and cold-rolled austenitic EN 1.4301 and hot-rolled lean duplex EN 1.4482, with B500C carbon steel rebars tested for comparison. Rebars of 12 mm and 16 mm diameter were tested across slenderness ratios $L/D = 5, 8, 10, 12, 15$ to capture the influence of inelastic buckling and strain amplitude on cyclic behaviour. The uniaxial material models were calibrated using truss and beam-column rebar representations, suitable for fibre-based and continuum modelling of reinforced concrete structures. The *Hysteretic* model is recommended for fibre-based simulations, as it more accurately reproduces the experimental response, with mean peak tensile and compressive stress errors of 1 % and -7 %, respectively. Conversely, *Steel02* is more suitable for continuum simulations, as it better captures geometric and nonlinear effects under cyclic loading, yielding mean peak tensile and compressive stress errors of -0.1 % and 3 %, respectively. Numerical simulations of reinforced concrete columns subjected to cyclic loading were conducted to validate the calibration methodology, confirming its robustness and the suitability of the calibrated parameters for accurate nonlinear and parametric modelling of reinforced concrete structures.

1. Introduction

The accuracy and reliability of numerical models of reinforced concrete structures depend heavily on the accurate representation of both the geometric and material characteristics of the structural components. Fibre-based modelling, implemented in several software programs such as OpenSees [1], SeismoStruct [2] and SAP2000 [3] is used to simulate reinforced concrete structures under monotonic and cyclic loading conditions. Modelling at one-, two- or three-dimensional levels is supported, allowing for varying levels of complexity in simulations. Within a distributed plasticity approach via fibre sections, the cross-section of a structural component is divided into individual fibres, each assigned a uniaxial material model that describes its stress-strain response. For example, fibre sections used to model the cross-section of a reinforced concrete member include uniaxial materials that define the stress-strain relationships for steel rebar, confined concrete (concrete core) and unconfined concrete (concrete cover).

In standard fibre-section beam-column models of reinforced concrete structural components, steel reinforcement is represented by

* Corresponding author. Faculty of Engineering and Physical Sciences, University of Southampton, UK.

E-mail address: h.t.m.moodley@soton.ac.uk (H. Moodley).

uniaxial fibres at the section level, without lateral degrees of freedom. Consequently, local reinforcement buckling between ties cannot be captured kinematically and must instead be represented indirectly through constitutive models, for example, by adopting steel rebar material models with compression softening and cyclic degradation, calibrated against tests that exhibit inelastic buckling and low-cycle fatigue effects. For such calibration, engineers commonly employ an isolated rebar modelled as a truss element with appropriate lateral restraint to reproduce the experimental response. In continuum modelling studies that explicitly simulate bar bending between ties, rebars may be modelled using beam-column elements with initial imperfections and support springs. In these cases, rebar material calibration is often supplemented by matching member-level tests to account for confinement, bond-slip, strain penetration and cyclic degradation.

Limited studies exist on simulating stainless steel-reinforced concrete structural components in OpenSees [4–6]. This scarcity is largely due to the limited availability of experimental cyclic stress-strain data for stainless steel rebars, which has hindered the development of calibrated uniaxial material models and dedicated hysteretic phenomenological formulations, despite clear evidence from monotonic and fatigue studies [7–11] that stainless steel rebars exhibit fundamentally different mechanical behaviour from carbon steel, including a rounded stress-strain response without a distinct yield point, higher ultimate-to-yield strength ratios, and enhanced ductility, necessitating constitutive models specifically calibrated for stainless steel behaviour.

Phenomenological cyclic stress-strain models for carbon steel rebars have been proposed in the literature, which are constructed from observations of rebar tests conducted under various loading conditions, using either experimental data or numerical modelling results. Furthermore, such models incorporate empirical relationships that capture the material and geometric properties of rebars and include rules specifying when each relationship should be applied. Two recent examples include the models developed by Han et al. [12] and Kashani et al. [13] for high-strength and corroded carbon steel rebars, respectively. However, implementing such phenomenological models in OpenSees can be challenging. This complexity is often avoided by utilising one of the many well-established uniaxial material models available in OpenSees. Recent studies, such as those by Carreno et al. [14] and DiSarno et al. [15], have demonstrated how existing uniaxial material models can be adapted to represent the stress-strain behaviour of carbon steel rebars. These investigations employed optimisation techniques to identify the most suitable set of parameters for the assessed uniaxial material models, ensuring an accurate representation of rebar behaviour. However, neither phenomenological nor calibrated uniaxial carbon steel rebar models are applicable to stainless steel, as both are based on carbon steel cyclic data; stainless steel specific cyclic datasets and OpenSees calibration are therefore required.

To address the identified knowledge gaps, this paper pursues two main objectives. The first objective is to generate the currently lacking experimental data on the cyclic stress-strain behaviour of stainless steel rebars. This is achieved through an extensive testing programme aimed at characterising the cyclic response of rebars with varying slenderness ratios and subjected to different strain amplitudes. The tested specimens include hot-rolled (HR) and cold-rolled (CR) 12 mm diameter austenitic EN 1.4301 and hot-rolled 16 mm diameter lean duplex EN 1.4482, with B500C carbon steel rebars tested for comparison. Monotonic tensile and compressive tests are also conducted to enable comparison with the corresponding cyclic backbone curves. The second objective is to develop calibrated uniaxial material models in OpenSees for stainless steel rebars based on the results of these newly conducted tests, and to validate their applicability by integrating them into reinforced concrete column models, advancing beyond previous studies by explicitly capturing cyclic degradation and inelastic buckling effects.

The paper begins with a description of the rebar cyclic and monotonic tests and the results obtained. This is followed by an overview of modelling approaches for steel rebars in OpenSees within the framework of fibre-based and continuum reinforced concrete component models. The uniaxial material models typically used to define the rebar behaviour, namely the *Steel02* and *Hysteretic*, are briefly presented. The development of truss and beam-column isolated steel rebar models in OpenSees, which are required to simulate rebar behaviour and thus enable calibration of the uniaxial model parameters, is described. The calibration process, based on rebar test results and a Particle Swarm Optimisation technique, is described. The model calibration results for stainless and carbon steel rebar of varying length-to-diameter ratios under cyclic loading are presented and discussed. Finally, numerical simulations of stainless-steel- and carbon-steel-reinforced concrete circular columns under cyclic loading using the described rebar cyclic modelling approaches are presented.

2. Experimental investigation

2.1. Test specimens

A test programme was conducted to characterise the monotonic tensile, monotonic compressive and cyclic stress-strain behaviour of ribbed stainless steel rebars, as summarised in Table 1. Hot-rolled (HR) and cold-rolled (CR) 12 mm diameter austenitic EN 1.4301

Table 1
Summary of experimental monotonic and cyclic tests.

Grade	Rebar diameter	Monotonic tension (No. Of tests)	Monotonic compression (L/D, No. Of tests per L/D)	Cyclic (L/D, No. Of tests per L/D)
EN 1.4301-CR	12 mm	2	5, 8, 10, 12 & 15 (2)	5, 8, 10, 12 & 15 (1)
EN 1.4301-HR	12 mm	2	5, 8, 10, 12 & 15 ^a (2)	5, 8, 10, 12 & 15 (1)
EN 1.4482-HR	16 mm	2	5, 8, 10, 12 & 15 (2)	5, 8, 10, 12 & 15 (1)
B500C	12 mm	2	5, 8, 10, 12 & 15 (2)	5, 8, 10, 12 & 15 (1)
B500C	16 mm	2	5, 8, 10, 12 & 15 (2)	5, 8, 10, 12 & 15 (1)

^a for this L/D, one test was performed.

Table 2
Mill certificate chemical composition of tested stainless steel rebars (%).

Grade	C	Si	Mn	Cr	Mo	Cu	Ni	P	S	N	Ti
EN 1.4301-CR	0.057	0.400	1.58	18.07	0.300	0.470	8.01	0.036	0.001	0.060	0.005
EN 1.4301-HR	0.020	0.490	1.76	18.40	–	–	8.10	0.033	0.001	0.210	–
EN 1.4482-HR	0.057	0.615	4.19	20.23	0.412	0.176	1.82	0.024	0.001	0.148	0.013

Table 3
Mill certificate tensile properties of tested stainless steel rebars.

Grade	$R_{p,0.2}$ (MPa)	R_m (MPa)	A_{gt} (%)	A_5 (%)
EN 1.4301-CR	670	853	18	30
EN 1.4301-HR	559	813	12	34
EN 1.4482-HR	581	815	32	42

and hot-rolled 16 mm diameter lean duplex EN 1.4482 stainless steel rebars were investigated. The rebars were manufactured in Europe in accordance with the EN 10088 [16] material product standard. The tested diameters are widely used in seismic Mediterranean countries [17,18], with 16 mm and 12 mm diameters used in beams as primary and secondary flexural reinforcement, respectively; 16 mm diameters are used as secondary rebars in columns for combined axial-flexural strength, together with the 20 mm diameter rebar in low-to medium-rise frame structures. Additionally, carbon steel B500C rebars of the same diameter were tested for comparison.

The stainless steel rebars tested have different surface finishes, rib patterns, corrosion resistance and mechanical properties, with the latter two primarily determined by the material's chemical composition. The chemical compositions and tensile properties of the rebars, as provided by the mill certificates, are presented in Tables 2 and 3, respectively. In Table 3, $R_{p,0.2}$ is the 0.2 % proof stress, R_m is the ultimate tensile stress, A_{gt} is the total elongation at maximum force, and A_5 is the elongation after fracture. The austenitic EN 1.4301 and lean-duplex EN 1.4482 grades, classified as Stainless Steel Resistance Class SSRC2 by EN 1992-1-1 [19] based on their pitting resistance equivalent values, are considered suitable for most atmospheric and concrete cover environments. Lean-duplex grades are more cost-effective due to their lower initial material cost, associated with reduced Ni alloying content, typically 1.82 % compared with approximately 8 % in austenitic grades.

2.2. Test methodology

Monotonic tensile tests were conducted to measure the fundamental uniaxial stress-strain response of the rebars, in accordance with EN 6892-1 [20]. The full details of the tensile test setup and instrumentation employed are reported by the authors in Moodley, Afshan & De Risi [8], where the same rebars were investigated under low-cycle high-amplitude fatigue. Monotonic compressive tests were performed herein to investigate the effect of rebar slenderness on the stress-strain response under uniaxial compression. Although rebars in reinforced concrete members are encased in concrete, rebar buckling remains a critical consideration under cyclic loading conditions. Inelastic buckling may occur in regions of high plastic demand where concrete cover spalls and transverse confinement is reduced or insufficient. Experimental and post-earthquake observations have shown that longitudinal bars can experience instability, particularly between widely spaced ties, over multiple tie spacings if transverse reinforcement stiffness is inadequate or after degradation of concrete confinement. Therefore, to ensure accurate representation of cyclic behaviour in numerical models, it is essential to account for the effects of bar slenderness and post-buckling response at the material level. This study includes rebar tests over five length-to-diameter slenderness (L/D) ratios ($= 5, 8, 10, 12, 15$) to calibrate material models that capture geometric instability effects, representing typical tie spacings or buckling lengths in reinforced concrete columns [21].

The tests were performed using a 630 kN Schenck servo-hydraulic testing machine under displacement control at a constant strain rate of 0.005 strain/s up to a maximum applied strain of 20 %. In total, 49 monotonic compressive tests were conducted, including two repeat tests for each rebar material and L/D ratio, except for EN 1.4301-HR $L/D = 15$, where material availability limited testing to a single test. Compressive stress and strain were measured during the tests. Stress was calculated as the applied load, measured by the internal machine load cell, divided by the rebar cross-sectional area, taken as 113 mm² and 201 mm² for 12 mm and 16 mm rebars, respectively. Strain was measured using a dot-tracking imaging technique similar to that employed in Ref. [7], in which multiple dots were applied to the specimen, and images were captured at a rate of 2 Hz during the test. Two cameras were used: one directly facing the specimen and the other positioned at an angle of 120° relative to the front camera, as shown in Fig. 1, allowing a continuous view of the tracked dots regardless of the direction of rebar buckling. Both cameras were Manta-G504B models, equipped with Nikkor AF 50 mm $f/1.8D$ lenses for the $L/D = 10, 12$ and 15 rebars, and Sigma 105 mm $f/2.8D$ lenses for the $L/D = 5$ and 8 rebars. The acquired images were processed to track the applied dots subpixels using the Plugin TrackMate [22] within the open-source image processing software Fiji-ImageJ [23]. The longitudinal compressive strain between a pair of selected dots at an initial distance of L_0 was computed as the change in distance between the dots [in pixels] divided by the original distance between the dots [in pixels].

A total of 25 cyclic tests were performed on the same rebar grades and L/D ratios. The tests were conducted in a 250 kN Instron servo-hydraulic testing machine under displacement control at a constant rate of 0.005 strain/s. The cyclic loading protocol involved a

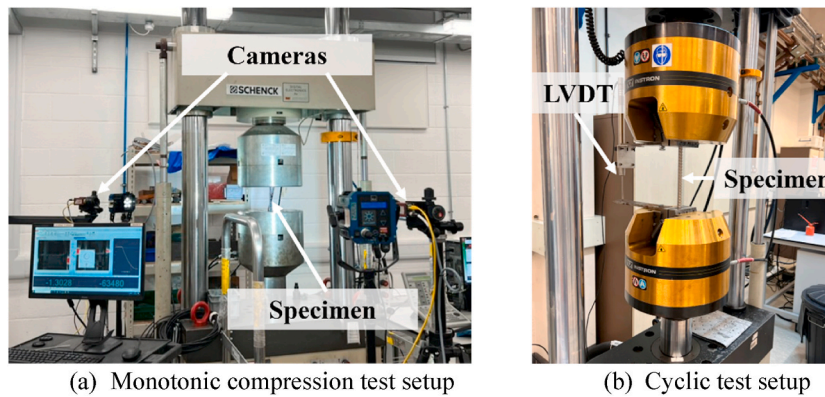


Fig. 1. Monotonic compression and cyclic test setups.

double-cycle reversed symmetric pattern with peak strain amplitudes of 1 %, 2 %, 3 %, 4 % and 5 %. A dot tracking system, identical to that described for the compressive tests, along with a Linear Variable Displacement Transducer (LVDT) with a stroke of ± 50 mm, connected between the top and bottom of the testing machine grips, as depicted in Fig. 1, was used to measure the average strain over the parallel length of the rebars. After confirming consistent results from both measurement methods and demonstrating effective gripping of the rebar ends, the LVDT was used for all cyclic tests, similar to the rebar cyclic test setups in the literature [12,24].

2.3. Measured stress-strain responses

The cyclic stress-strain responses of the stainless steel rebars are shown in Fig. 2, together with the monotonic tensile and compressive curves for comparison with the corresponding cyclic backbone curves. In all cyclic stress-strain plots, tension is taken as positive and compression as negative. The cyclic responses of the carbon steel rebars tested for comparison are provided in Appendix A. The mean and coefficient of variation (COV) of the key measured tensile mechanical properties are reported in Table 4, where E is the Young's modulus, f_y is the yield stress, taken as the 0.2 % proof stress $f_{0.2}$ for stainless steel rebars, f_u is the ultimate tensile stress, ϵ_u is the strain at the ultimate tensile stress and $\epsilon_{f,pl}$ is the fracture strain. For $L/D = 5$, the cyclic response is initially symmetric at low strain amplitudes ≤ 2 %, but becomes asymmetric beyond ≥ 3 % due to inelastic buckling, causing progressive compressive softening, while tensile cycles remain stable. At higher slenderness ratios, responses are dominated by inelastic buckling and geometric nonlinearities, producing asymmetric loops and pinching during compression-tension reversals. These effects become increasingly pronounced with increases in both L/D and strain amplitude. Across all L/D values, compressive cyclic backbones resemble monotonic curves, but with greater stress degradation due to the Bauschinger effect and prior tensile straining. Tensile backbones generally follow the monotonic response, with rebars with $L/D \geq 8$ following this response up to approximately 2–3 % strain before strength degradation occurs. Repeat cycles at each strain amplitude generally produced lower peak stresses than the first, reflecting fatigue-related softening.

3. Modelling of rebars in OpenSees

3.1. Steel rebar modelling approaches in OpenSees

In standard fibre-section modelling of reinforced concrete members, which is widely employed for its computational efficiency and simplicity [25], the section is discretised into unconfined concrete, confined concrete and steel reinforcement fibres, each assigned a calibrated uniaxial material model, as illustrated in Fig. 3. Since fibres have no explicit geometric definition, the effects of rebar slenderness (L/D) and associated geometric nonlinearities are incorporated through the adopted stress-strain models. Calibration is performed against experimental stress-strain data for rebars with the same slenderness, which inherently include the effects of geometry, by developing an isolated rebar model in OpenSees, typically as a truss element, and iteratively fitting the material parameters. Recent advances in the Scientific Toolkit for OpenSees (STKO) [26] have enabled more sophisticated modelling of reinforced concrete using continuum elements for concrete and force- or displacement-based beam-column elements for reinforcement, as shown in Fig. 4. Similar to the fibre-section modelling approach, uniaxial material models are used for steel rebars, but their parameters are calibrated using isolated beam-column rebar models fitted to experimental data that capture the effects of geometric nonlinearities.

3.2. OpenSees uniaxial material models

A variety of uniaxial material models are available in the OpenSees material library. This paper considers two commonly used uniaxial material models, *Steel02* and *Hysteretic*, to represent the stress-strain behaviour of steel rebars in reinforced concrete structures. The development and full descriptions of these models are reported in the literature [14,27–29] and the OpenSees user manual [1]. A brief overview of each model necessary for the subsequent calibration is presented herein.

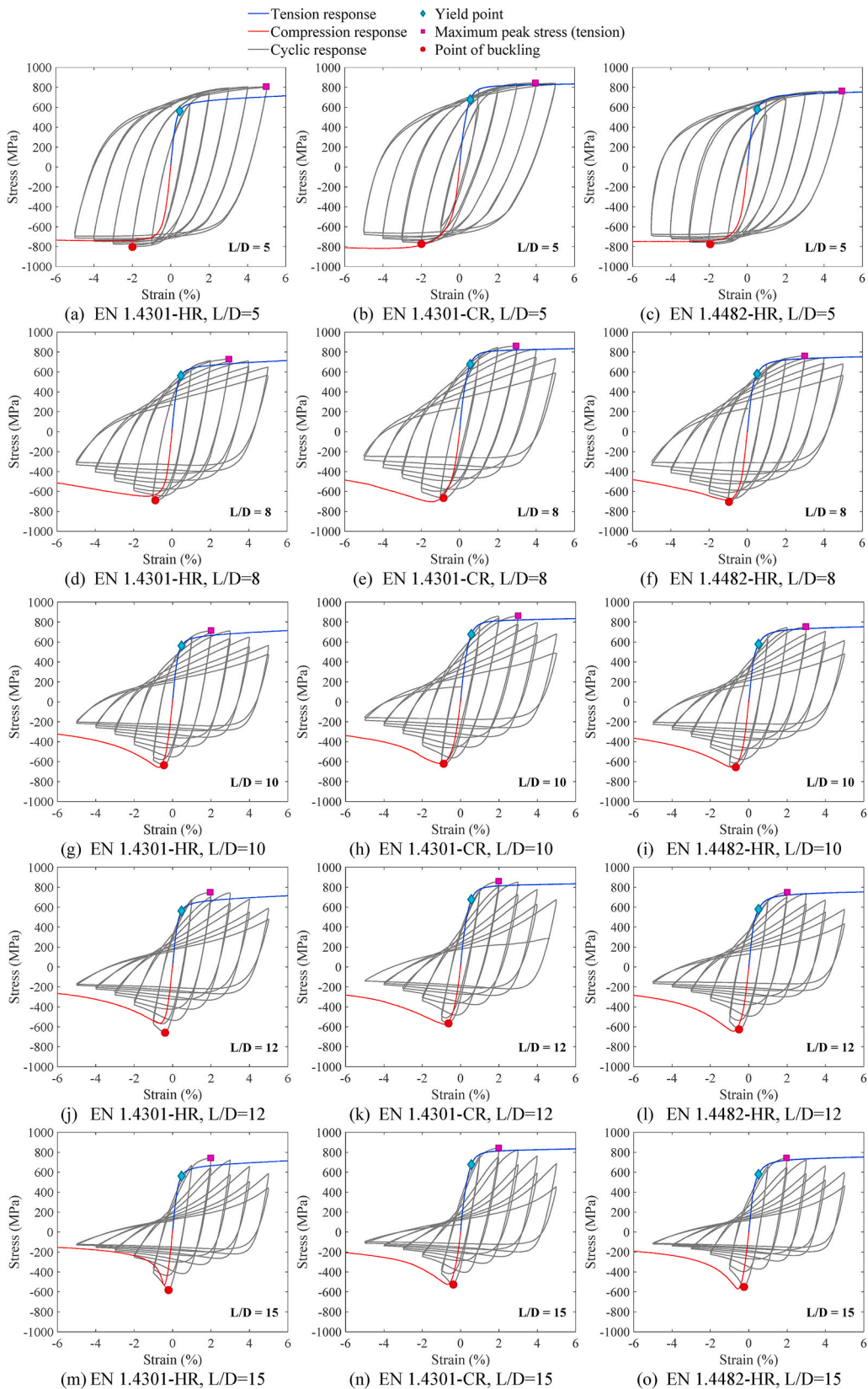


Fig. 2. Measured cyclic stress-strain responses of stainless steel rebars.

Table 4
Key measured tensile mechanical properties.

Specimen	Statistic	E (N/mm ²)	f _y (N/mm ²)	f _u (N/mm ²)	ε _u (%)	ε _{f,pl} (%)
EN 1.4301-CR	Mean	207500	677	872	21.75	35
	COV (%)	1.7	4.0	0.3	2.3	3.2
EN 1.4301-HR	Mean	195000	562	818.5	29.5	49.6
	COV (%)	3.6	3.0	0.4	6.2	6.0
EN 1.4482-HR	Mean	200000	578.5	827	36.2	45.3
	COV (%)	7.1	0.6	0.2	2.0	4.7
B500C-12 mm	Mean	200000	560	657	11.4	–
	COV (%)	4.9	1.8	1.3	14.9	–
B500C-16 mm	Mean	195500	594	681.5	8.665	–
	COV (%)	0.4	0.7	0.5	3.0	–

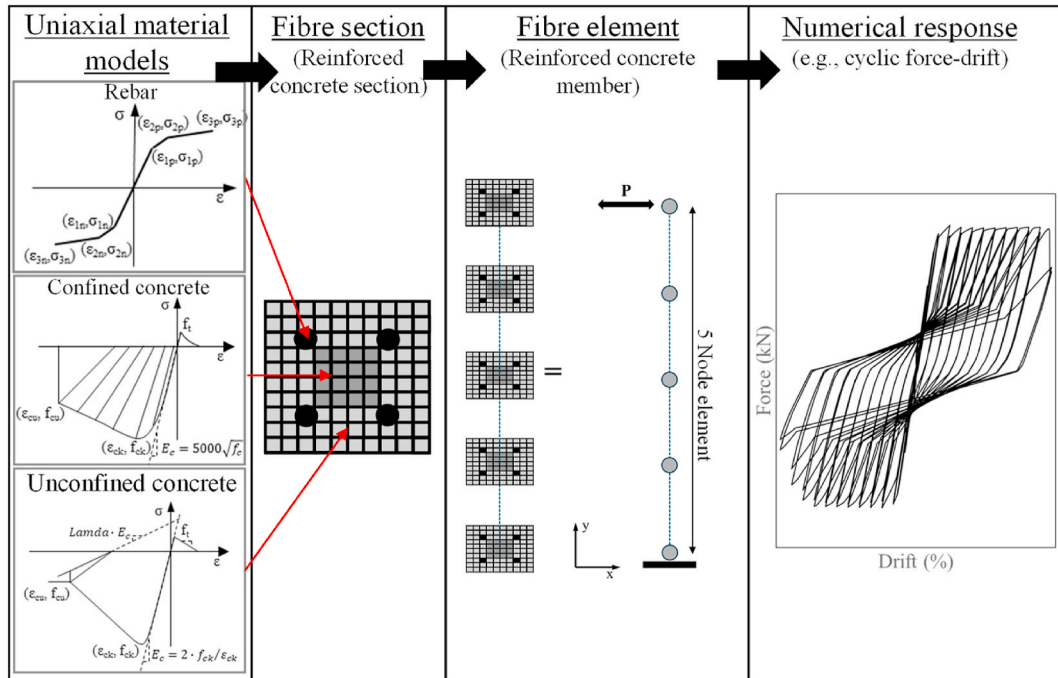


Fig. 3. Schematic of fibre-section modelling of a reinforced concrete component.

3.2.1. Steel02 uniaxial material model

Steel02 is a uniaxial material model based on the Giuffre-Menegotto-Pinto formulation [27] with isotropic strain hardening. It features a bilinear stress-strain response, with an initial slope E equal to the material's Young's modulus, a hardening slope of bE , where b is the post-yield strain hardening ratio, and a smooth transition curve of radius R_0 between the elastic and plastic stages, as shown in Fig. 5. For cyclic loading, the parameters that control the shape of the transition curve are R_0 as well as cR_1 and cR_2 , which control the curvature variation of the Bauschinger curve following each strain reversal. The model assumes isotropic hardening to model the evolution of the yield surface with respect to plastic deformation, as controlled by the a_1 and a_2 isotropic hardening parameters for compression loading, and the a_3 and a_4 isotropic hardening parameters for tension loading.

3.2.2. Hysteretic uniaxial material model

The *Hysteretic* uniaxial material model employs a quad-linear stress-strain relationship, representing a range of structural materials or components. The model consists of tensile and compressive quad-linear backbone curves, defined by three user-defined points in each loading direction, which consist of (i) the initial elastic stage up to the defined yield point (ϵ_1, σ_1) followed by (ii) the first intermediate stage to the defined intermediate point (ϵ_2, σ_2) and (iii) the second intermediate stage up to the defined ultimate point (ϵ_3, σ_3) and a final (iv) post-ultimate stage. As the *Hysteretic* uniaxial material model requires both a backbone curve in tension and compression, three sets of stress-strain parameters must be defined for tension ($\epsilon_{1p}, \sigma_{1p}, \epsilon_{2p}, \sigma_{2p}, \epsilon_{3p}, \sigma_{3p}$) and compression ($\epsilon_{1n}, \sigma_{1n}, \epsilon_{2n}, \sigma_{2n}, \epsilon_{3n}, \sigma_{3n}$), as shown in Fig. 6a. Furthermore, the *Hysteretic* model includes five additional parameters: *PinchX*, *PinchY*, *Damage1*, *Damage2* and β_{mu} . Pinching in the *Hysteretic* model refers to the reduction in stress and stiffness during unloading and reloading in the cyclic response. The *PinchX* and *PinchY* parameters are pinching factors used to define the strain and stress during reloading,

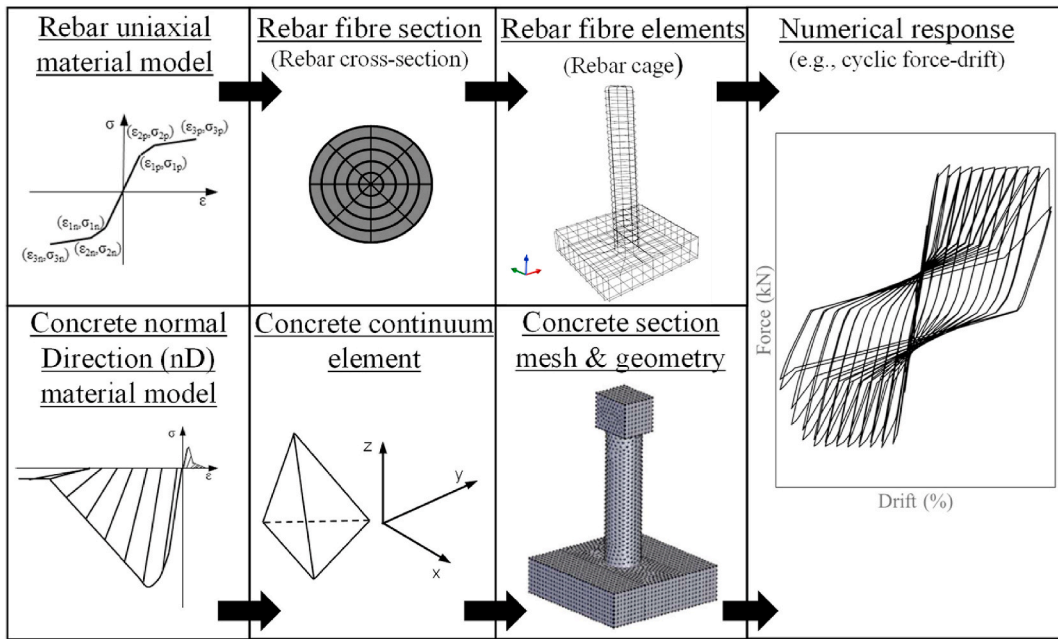


Fig. 4. Schematic of continuum modelling of a reinforced concrete component in STKO.

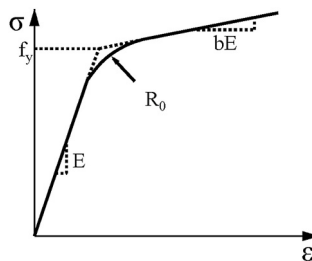


Fig. 5. Schematic of the *Steel02* uniaxial material model monotonic curve.

respectively, as illustrated in Fig. 6b. The *PinchX* and *PinchY* values range from 1 to 0, with smaller values representing a more severe pinching effect. The impact of the relative values of the *PinchX* and *PinchY* parameters on the cyclic response envelope is illustrated in Fig. 6c. In the *Hysteretic* model, two damage parameters are used to model the strength degradation due to cyclic loading. The strength-reducing damage parameters *Damage1* and *Damage2*, depend on ductility and energy, respectively. For *Damage1*, the reduction in strength is proportional to the applied strain level, with greater damage occurring at higher strain levels. Similarly, strength reduction due to *Damage2* is proportional to the energy dissipated by the inelastic strain, with the reduction increasing as the number of cycles at a fixed strain level increases.

4. Development of rebar models in OpenSees and optimisation procedure

4.1. Development of steel rebar models

To calibrate the parameters for the selected steel rebar material models (e.g., *Steel02* or *Hysteretic*), an isolated rebar was first modelled in OpenSees and assigned the corresponding material definition. The model parameters were then determined iteratively using an optimisation procedure to achieve an acceptable match between the experimentally measured stress-strain response and the OpenSees simulation results, as detailed in the following sections. A truss element model of a steel rebar was constructed between two end nodes, as shown in Fig. 7a. The top node was fixed, while the bottom node, where the load was applied, was free to move in the axial direction. The element had a non-dimensional length and area equal to unity. Hence, displacement was applied directly as strain and stress were output directly from the model. This modelling strategy is similar to the method used in the material testing script included in OpenSees [1]. Similarly, a beam-column element model with distributed plasticity and a force-based formulation was developed to represent the steel rebar, as shown schematically in Fig. 7b. The total rebar length was divided into six equal-length force-based beam-column elements. Five Gauss-Lobatto integration points were defined, to which the steel rebar material model

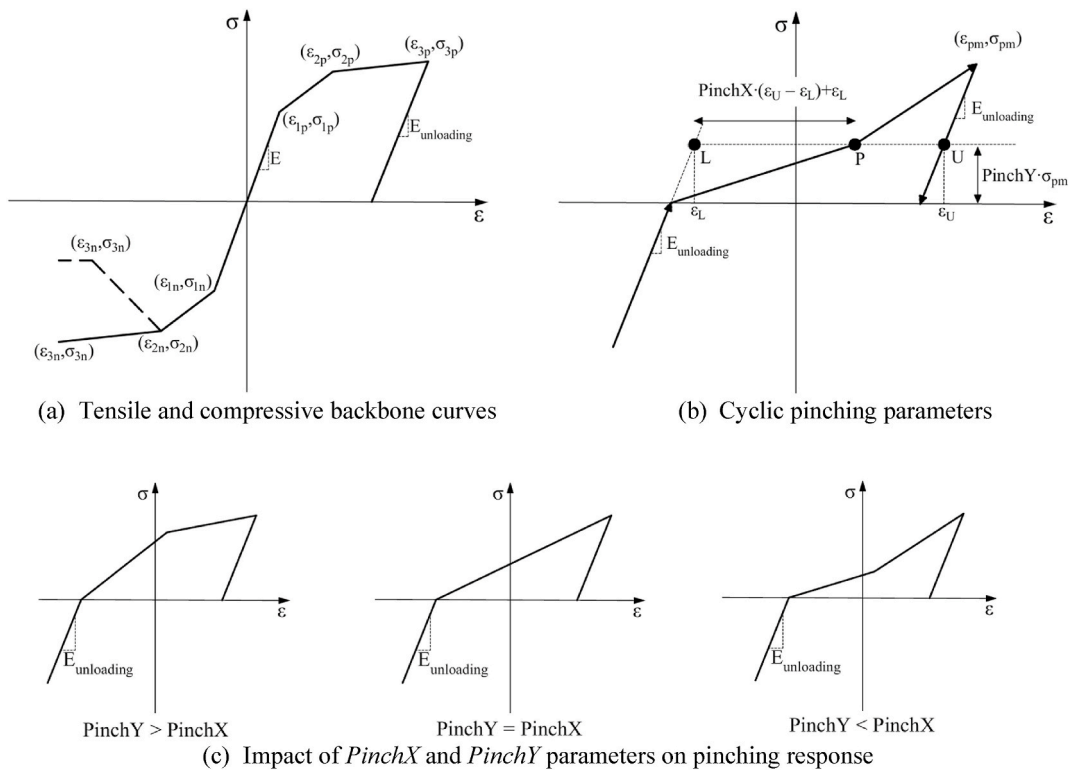


Fig. 6. Schematic of the *Hysteretic* uniaxial material model.

was assigned. Each integration point comprised circular fibre-sections with 8 radial and 25 circumferential fibres. The fibre arrangement was determined through mesh sensitivity analysis to balance computer efficiency and accuracy. To simulate buckling, a global imperfection in the form of a half-sine wave with a maximum amplitude of $L/1000$, where L is the total rebar length, was applied to the model. This imperfection has been successfully adopted in previous modelling studies of reinforcing steel [7,15,30]. Boundary conditions were used to simulate the experimental rebar end conditions. All displacement and rotational boundary conditions at the top and bottom nodes of the rebar were fixed, except for the vertical displacement at the bottom node, where the load was applied. The Corotational Transformation command in OpenSees was used to capture the effects of geometric nonlinearities arising from large displacements and rotations. For both the truss and beam-column models, an adaptive convergence algorithm was employed, initially using the *KrylovNewton* solution method with a predefined loading step that was progressively reduced to a threshold to achieve convergence. If convergence still failed, the solution algorithm was switched to *Newton*, *ModifiedNewton* or *NewtonLineSearch*.

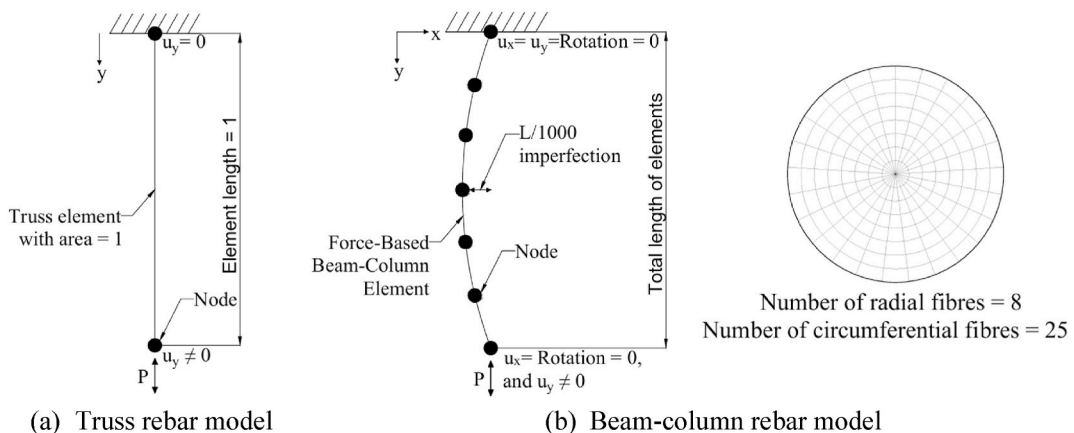


Fig. 7. Schematic of truss and beam-column isolated steel rebar models.

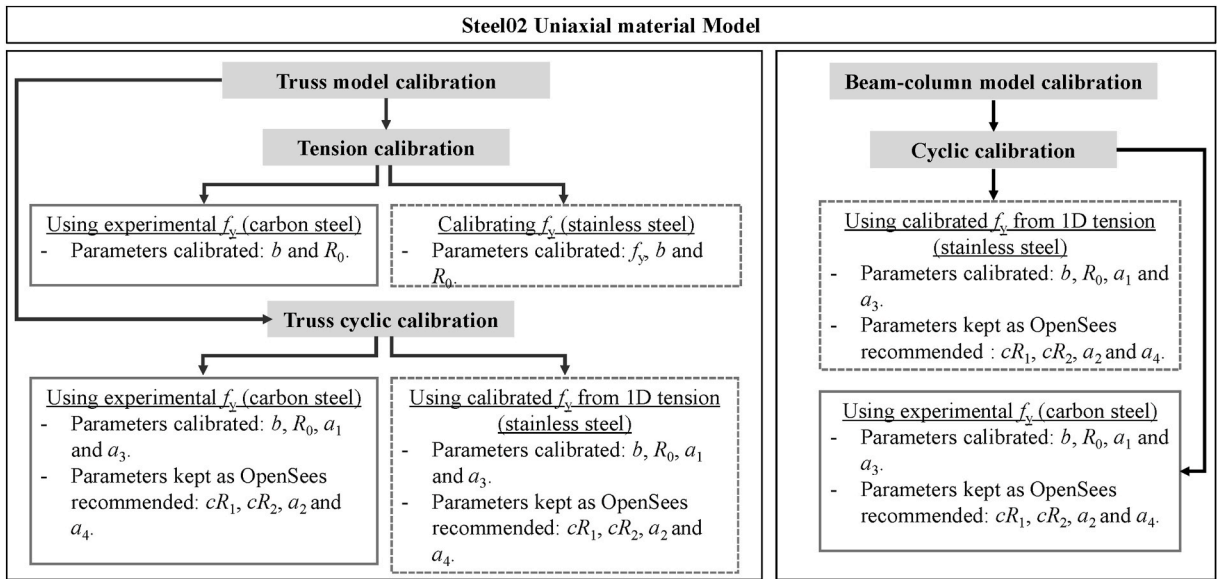


Fig. 8. Steel02 material model calibration process.

4.2. Calibration of uniaxial material model parameters

4.2.1. Steel02 material model parameters

The truss and beam-column models described in Section 4.1 were used to simulate the steel rebars under different loading conditions, with the Steel02 uniaxial material model assigned to them. The aim was to calibrate the Steel02 cyclic material model by optimising its parameters to achieve the best fit with the experimentally measured responses. An overview of the calibration process is presented in Fig. 8. For the calibration of the truss Steel02 cyclic models, the model parameters b and R_0 , along with the isotropic hardening parameters a_1 and a_3 , were optimised. The other parameters, cR_1 , cR_2 , a_2 , and a_4 , were set to the default values recommended by OpenSees, equal to 0.925, 0.15, 1, and 1, respectively. A prior calibration of the tensile models was carried out to determine the yield stress f_y for the stainless steel rebars, as the conventionally defined 0.2 % proof stress did not accurately represent the yield stress definition in the Steel02 model, taken as the intersection between the initial linear elastic and strain-hardening parts of the stress-

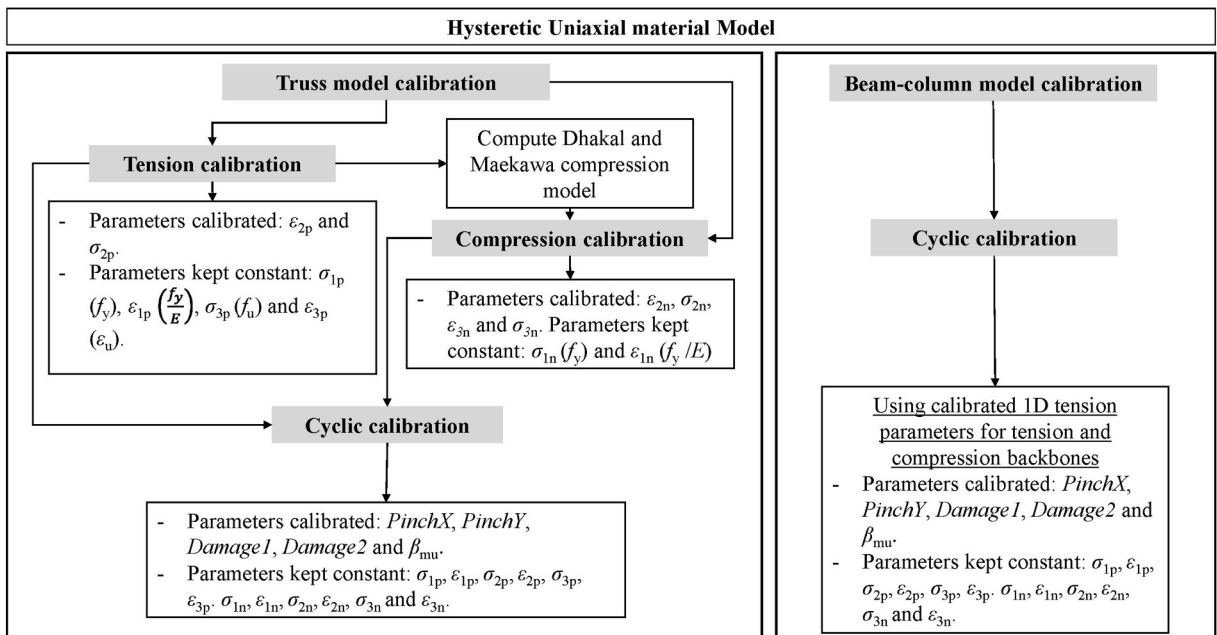


Fig. 9. Hysteretic material model calibration process.

strain response. For carbon steel rebars, the measured yield stress from the test responses was adopted directly. The upper and lower boundaries for the optimised a_1 , a_3 , b and R_0 were set to $[-0.5, 0.5]$, $[-0.5, 0.5]$, $[0, 0.1]$, $[4, 20]$, respectively. The beam-column *Steel02* cyclic model was calibrated in a similar approach as described above, with the exception of using different upper and lower ranges for the a_1 , a_3 , b and R_0 parameters equal to $[0, 0.1]$, $[0, 0.1]$, $[0, 0.02]$ and $[7, 20]$, respectively, to achieve better calibration.

4.2.2. Hysteretic material model parameters

The truss and beam-column models described in Section 4.1 were also used to simulate steel rebars with the *Hysteretic* uniaxial material model under different loading conditions, following the process presented in Fig. 9. For the truss *Hysteretic* models, tensile and compressive backbone curves were first obtained using calibrated tensile and compressive models. For the tensile backbone curve, the user-defined stress-strain points were taken as the experimental yield point (ϵ_y, f_y) and ultimate point (ϵ_u, f_u) for the first $(\epsilon_{1p}, \sigma_{1p})$ and third $(\epsilon_{3p}, \sigma_{3p})$ stress-strain points, respectively. The second $(\epsilon_{2p}, \sigma_{2p})$ stress-strain point was determined during calibration as a point between the experimental yield and ultimate points, such that the multi-linear stress-strain model closely matches the overall measured stress-strain response. The upper and lower boundaries for the optimised ϵ_{2p} and σ_{2p} parameters were set to (f_y, f_u) and (ϵ_y, ϵ_u) , respectively.

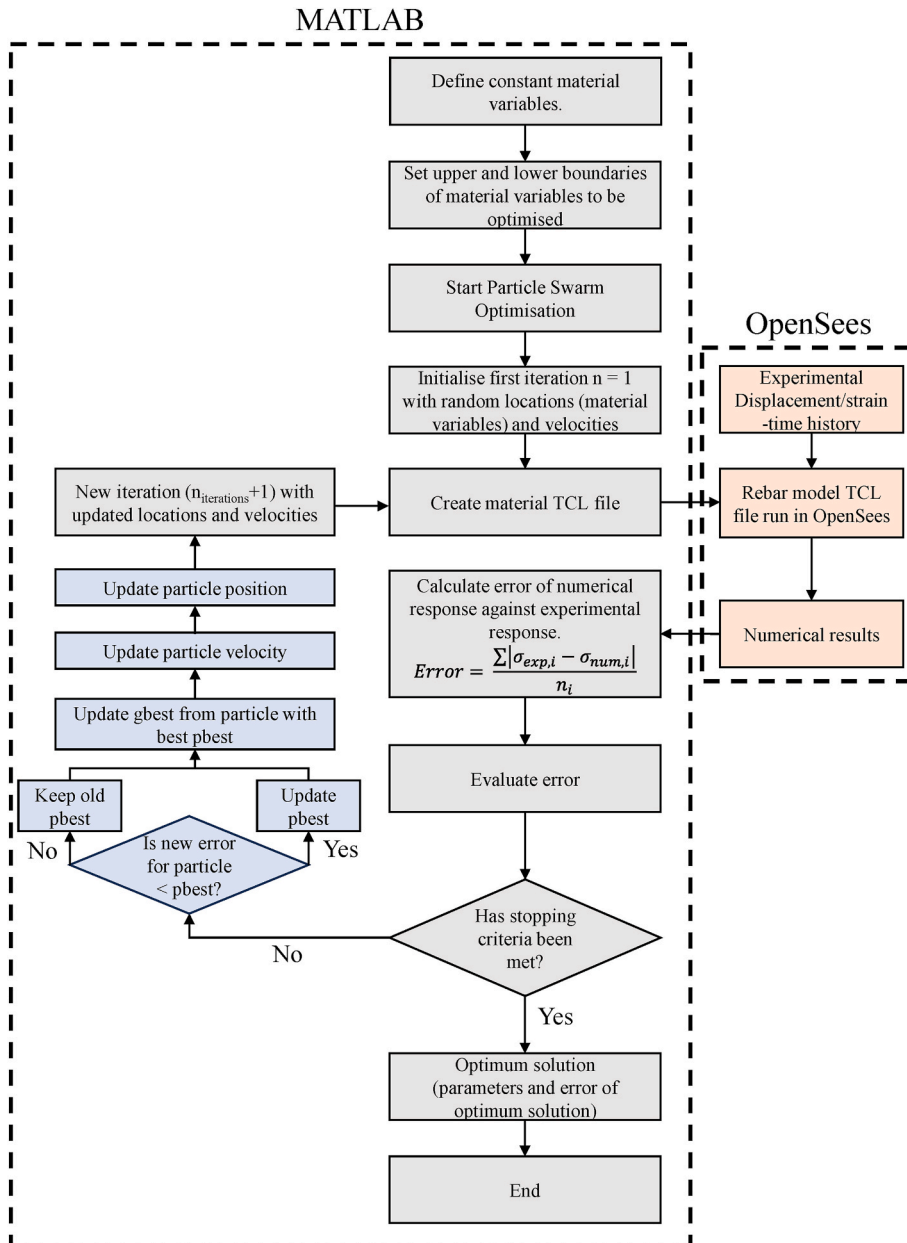


Fig. 10. Flowchart of Particle Swarm Optimisation (PSO) procedure.

For the compressive backbone curve, the effect of rebar inelastic buckling needed to be captured by selecting appropriate user-defined stress-strain points. Therefore, the rebar compressive model proposed by Dhakal and Maekawa [31] was adopted. The calibration process involved two steps: (1) computing the Dhakal and Maekawa model response for the tested rebar to simplify the nonlinear compressive stress-strain response to a multi-linear form, as in the *Hysteretic* model, followed by (2) calibrating the *Hysteretic* model parameters against the fitted Dhakal and Maekawa model. To fit the Dhakal and Maekawa model, a tensile stress-strain response was assumed, taken as the tensile backbone curve described above. The compressive backbone curve had the first stress-strain point (ϵ_{1n} , σ_{1n}) set to the yield stress point (ϵ_y , f_y), which represents the end of the first stage of the Dhakal and Maekawa model, while the other two stress-strain points (ϵ_{2n} , σ_{2n}) and (ϵ_{3p} , σ_{3p}) were optimised against the Dhakal and Maekawa model. The upper and lower boundaries of the two stresses were 0 and the maximum compressive stress σ_{max} , respectively, while the upper and lower boundaries of the two strains were ϵ_y and 0.15, respectively. In addition, to calibrate the *Hysteretic* truss cyclic model, the parameters *PinchX*, *PinchY*, *Damage1*, *Damage2* and β_{mu} , were optimised within the following upper and lower boundaries: [0.01, 1], [0, 1], [0, 0.8], [0, 1] and [0, 0.4], respectively.

For the calibration of the beam-column cyclic *Hysteretic* models, the calibrated tensile backbone parameters from the truss *Hysteretic* tension model were adopted. The beam-column rebar model does not require a compressive backbone curve, unlike the truss *Hysteretic* models, to represent the buckling effects. Instead, these effects are accounted for through geometric considerations within the model. Therefore, the input compressive backbone curve was assumed to be the same as the tensile one. The parameters optimised were: *PinchX*, *PinchY*, *Damage1*, *Damage2* and β_{mu} using the upper and lower boundaries: [0, 0.5], [0.3, 1], [0, 0.01], [0, 0.1] and [0, 0.6], respectively.

4.2.3. Optimisation procedure for model calibration

The Particle Swarm Optimisation (PSO) technique, available within MATLAB's optimisation toolbox [32], was employed for model calibration. The error was quantified using the mean absolute error (MAE), computed by interpolating the calibrated and measured stresses at equal strain intervals and averaging the absolute differences across all data points. For cyclic responses, the calculation was performed segment by segment between reversal points and then combined to obtain the total error. An OpenSees *TCL* script and MATLAB were used together to automate the calibration process. Once the *TCL* script for the uniaxial material was generated, MATLAB executed the rebar model in OpenSees using the specific uniaxial material script and the experimental displacement-time history. The resulting model response was compared against the experimental data to calculate the error, which MATLAB then used to update the parameter sets for the next iteration. This iterative process continued until the convergence criteria were satisfied. Fig. 10 presents a flowchart of the PSO optimisation procedure employed in the calibration process.

5. Material model calibration results and discussions

5.1. Steel02 and Hysteretic cyclic truss model results

The parameters of the *Steel02* and *Hysteretic* models were calibrated against the rebar test data presented in Section 2, following the calibration process described in Section 4.2. The calibrated parameters for the *Steel02* cyclic model were f_y , R_0 , b , a_1 and a_3 . The calibrated parameters for the *Hysteretic* cyclic model included the tensile backbone parameters (ϵ_{1p} , σ_{1p}), (ϵ_{2p} , σ_{2p}) and (ϵ_{3p} , σ_{3p}), compressive backbone parameters (ϵ_{1n} , σ_{1n}), (ϵ_{2n} , σ_{2n}) and (ϵ_{3n} , σ_{3n}) and the cyclic parameters *PinchX*, *PinchY*, *Damage1*, *Damage2* and β_{mu} . The experimental (Exp) and calibrated *Steel02* and *Hysteretic* responses for stainless steel rebars are presented in Fig. 11 and those for selected carbon steel are presented in Fig. 12 for comparison. The calibrated model parameters and MAE are provided in Appendix B Tables B.1, B.2 and B.3 for reference.

For both stainless and carbon steel rebars with $L/D = 5$, the *Steel02* cyclic models accurately capture the evolution of peak tensile stress up to 4 % strain, but slightly overpredict it at 5 %, particularly for 12 mm hot-rolled and cold-rolled EN 1.4301 rebars. Additionally, for all $L/D = 5$ cases, the *Steel02* model does not capture the experimentally observed compressive stress degradation and overestimates the unloading stiffness, although this discrepancy diminishes at higher strain amplitudes. Nevertheless, despite these discrepancies, the *Steel02* models generally capture the overall trend of the cyclic behaviour for $L/D = 5$ rebars. Since the *Steel02* model uses a single backbone curve for both tension and compression, it lacks a dedicated mechanism to capture buckling behaviour, such as pinching in compression. Moreover, because truss elements in OpenSees do not include geometric nonlinearities, fibre-section models cannot explicitly simulate buckling effects. However, at higher slenderness ratios, the *Steel02* models exhibit cyclic stress softening in both tension and compression, attributed to the negative calibrated values of the isotropic hardening parameters (a_1 and a_3) for loading in compression and tension, respectively. Although cyclic softening was captured, the higher-slenderness *Steel02* models underestimated the experimental peak tensile stresses beyond the first cycle and generally overestimated peak compressive stresses, resulting in an underprediction of the compressive peak stress degradation over the applied loading protocol (defined here as the drop in peak compressive stress in the last cycle relative to the first cycle). For each model, the mean percentage under- or overprediction was calculated by averaging the per-cycle peak-stress errors over the entire loading protocol; these per-model average errors ranged from -49 % to -5 % (mean: -25 %) in tension and from 5 % to 38 % (mean: 24 %) in compression, while the underestimation of peak compressive stress degradation was 35 % to 83 % (mean: 56 %).

For stainless and carbon steel rebars with $L/D = 5$, the *Hysteretic* cyclic models capture the overall stress-strain response, including the peak stress degradation in tension and compression and unloading stiffnesses at strain reversals. However, due to the linear nature of the *Hysteretic* model, it does not fully replicate the curvature of the experimental cycles. Additionally, for stainless steel rebars, the model does not entirely capture the cyclic strain hardening observed in the hot-rolled rebars. For rebars with $L/D \geq 8$, the *Hysteretic* models generally captured the overall experimental cyclic response, including tensile stress degradation and the stress at peak compressive strains. On a per-model basis (mean over all cycles), peak tensile stress errors ranged from -7 % to 11 % (mean: 1 %),

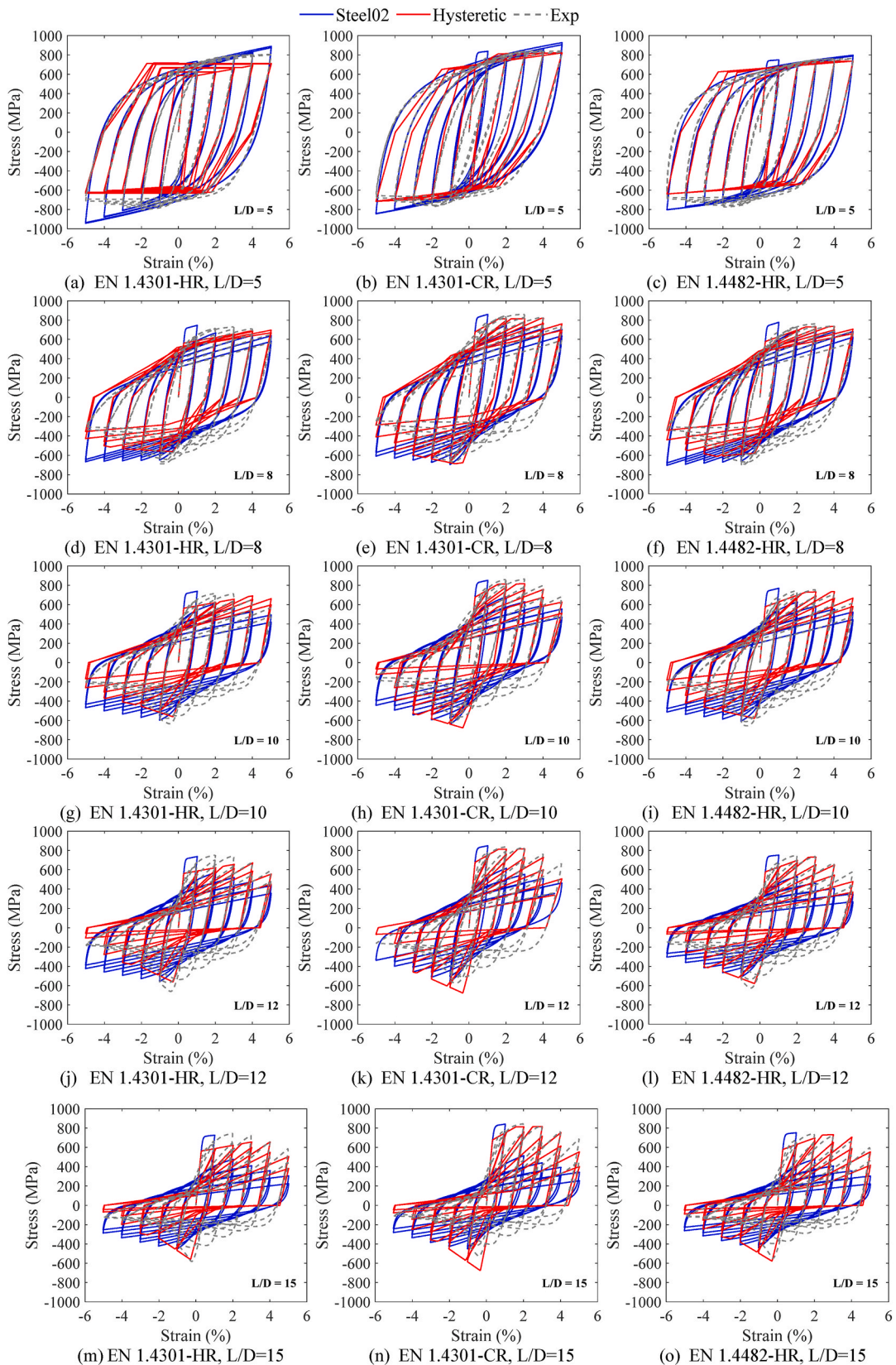


Fig. 11. Comparisons of Steel02 and Hysteretic truss models for stainless steel rebars.

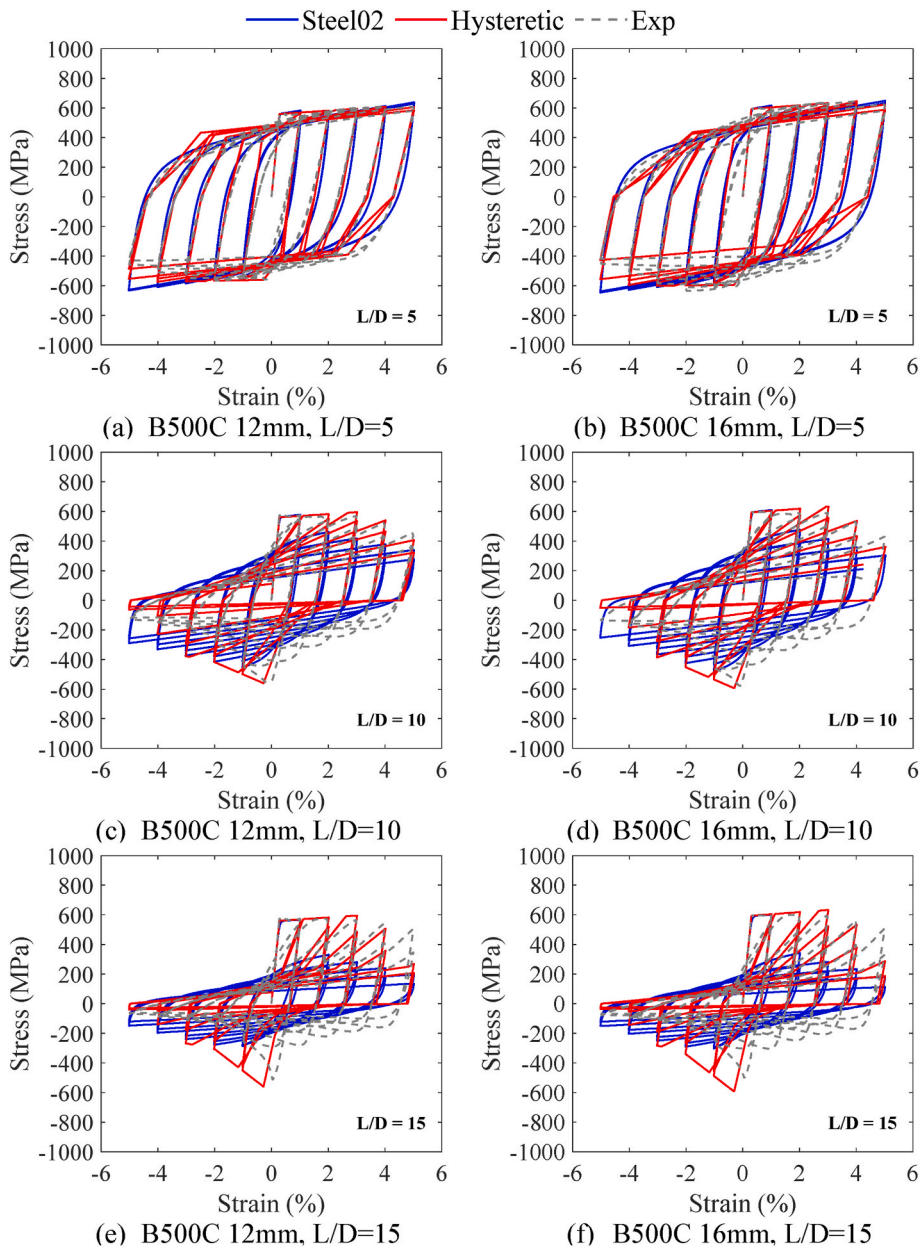


Fig. 12. Comparisons of *Steel02* and *Hysteretic* truss models for carbon steel rebars.

whereas peak compressive stress errors were larger, ranging from -23% to 10% (mean: -7%). Moreover, the compressive peak-stress degradation (compressive peak stress drop from first to last cycle) error ranged from -41% to 80% (mean: 21%). This is due to the pinching parameters controlling the narrowing of stress-strain loops caused by rebar buckling. Overall, the *Hysteretic* models were found to better capture the cyclic behaviour trends across a broader range of slenderness values and are considered appropriate for modelling rebars in fibre-based reinforced concrete structural components under cyclic loading.

5.2. *Steel02* and *Hysteretic* cyclic beam-column model results

The calibrated *Steel02* uniaxial material model parameters, obtained from beam-column rebar models that explicitly capture geometric nonlinearities, were f_y , R_0 , b , a_1 and a_3 . For the *Hysteretic* model, since the beam-column rebar models explicitly simulated the geometric buckling effects, only the tensile backbone curves needed to be defined, which were taken as those calibrated for the truss models. However, the cyclic parameters *PinchX*, *PinchY*, *Damage1*, *Damage2* and β_{mu} were calibrated on the basis of the beam-column rebar models. Comparisons of experimental (Exp) and calibrated numerical *Steel02* and *Hysteretic* cyclic stress-strain responses are shown in Figs. 13 and 14 for stainless steel and carbon steel rebars, respectively. The calibrated model parameters and MAE

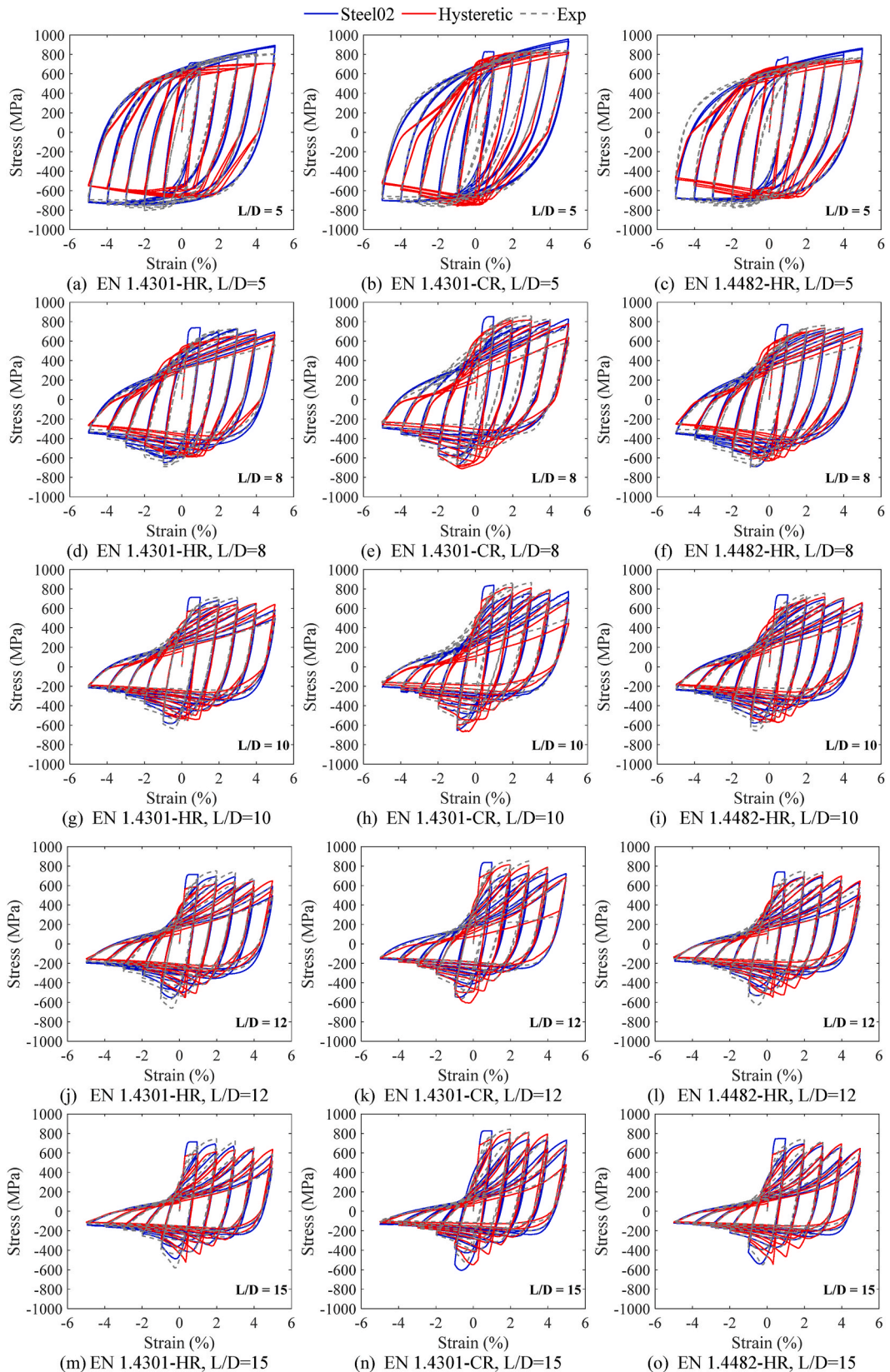


Fig. 13. Comparisons of *Steel02* and *Hysteretic* beam-column models for stainless steel rebar.

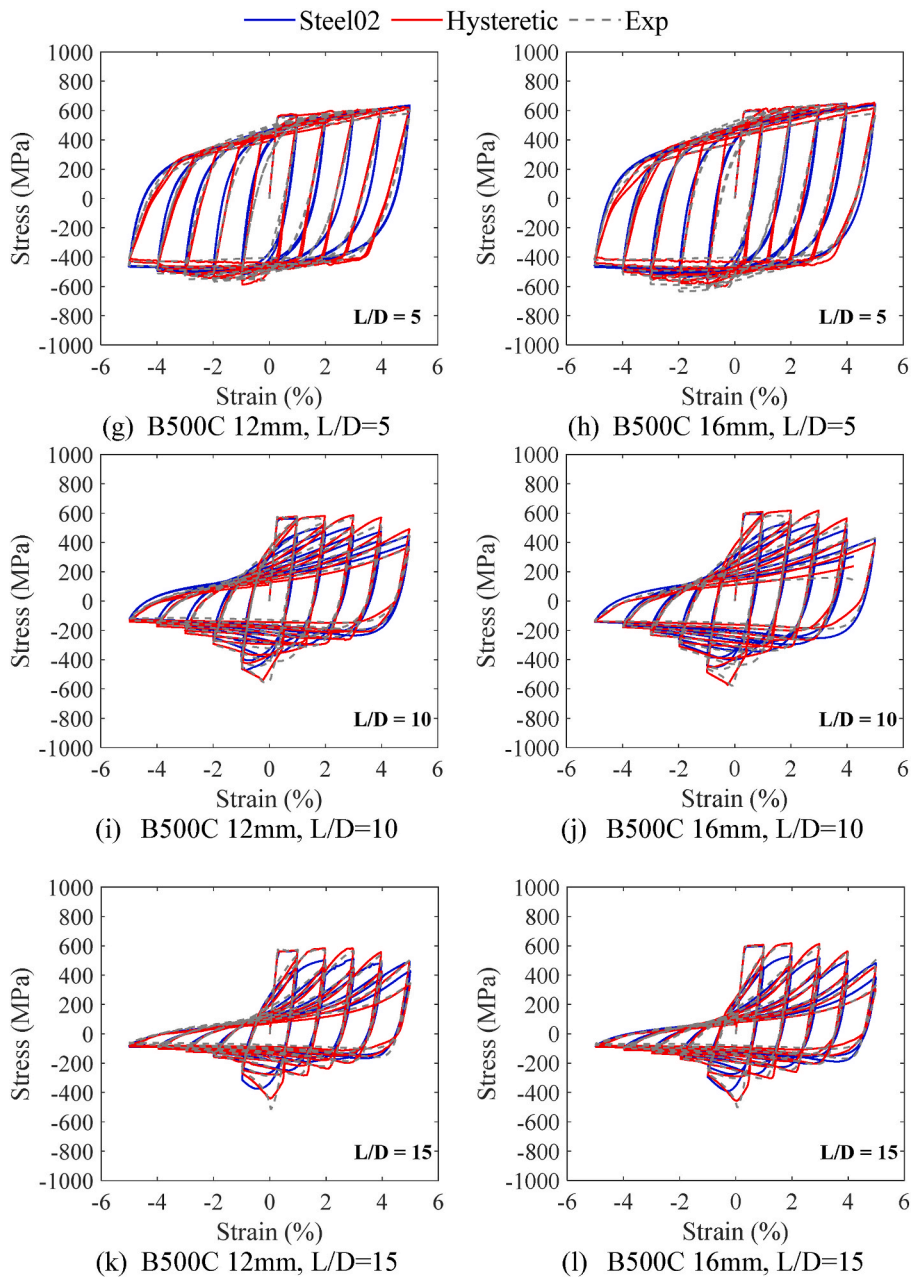


Fig. 14. Comparisons of *Steel02* and *Hysteretic* beam-column models for carbon steel rebars.

are provided in [Appendix B, Tables B.4 and B.5](#) for reference.

Since the beam-column *Steel02* cyclic models explicitly account for rebar geometric effects, such as inelastic buckling under compression, the calibrated cyclic stress-strain responses obtained from this approach are significantly more accurate than those from the simpler truss models across all L/D ratios. At L/D ratio of 5, the *Steel02* cyclic models are in good agreement with the experimental responses for both stainless and carbon steel rebars, capturing the general trend in behaviour, with minor discrepancies such as marginal underprediction of the peak compressive stresses in cycles with strain amplitudes $\leq 3\%$ for both rebars and an overprediction of peak tensile stresses in cycles with strain amplitudes $\geq 4\%$ for stainless steel rebars. For rebars with L/D ratios ≥ 8 , the general experimental stress-strain responses, including unloading and reloading stiffnesses and pinching in compression, are well captured. However, the peak tensile and compressive stresses are generally underestimated for both materials, particularly in cycles with strain amplitudes of 2% to 4%, while showing improvements at 5% strain amplitude, with per-model mean percentage errors (averaged over all cycles) in peak tensile and compressive stress ranging from -7% to 5% (mean: -0.1%) and from -12% to 14% (mean: 3%), respectively.

For the *Hysteretic* models, the calibrated cyclic stress-strain responses of stainless steel rebars showed some discrepancies compared to the experimental curves. For $L/D = 5$, the EN 1.4301-CR and EN 1.4482-HR models captured the peak tensile stress evolution, whereas the EN 1.4301-HR model did not reproduce the high levels of cyclic hardening in tension observed experimentally. At higher slenderness ratios, the models captured the overall response trends, with per-model mean percentage errors (averaged over all applied cycles) in peak tensile and compressive stress ranging from -5% to 0.1% (mean: -2.3%) and from -5% to 15% (mean: 5%), respectively. However, the models exhibited more pronounced pinching in compression than was recorded in the tests. These deviations are attributed to the multi-linear formulation of the *Hysteretic* model, which does not fully capture the nonlinearity and strain-hardening behaviour characteristic of stainless steel rebars. In contrast, the calibrated cyclic stress-strain responses of carbon steel rebars showed much closer agreement with the experiments. For $L/D = 5$, the models accurately reproduced the peak stresses in both tension and compression, as well as the degradation of compressive stress, although they did not capture the curved reloading behaviour observed in the experimental data. For more slender carbon steel rebars, the calibrated responses demonstrate good agreement with the experimental results, capturing peak tensile and compressive stresses over the applied loading protocol, with per-model mean percentage errors (averaged over all cycles) ranging from 0.2% to 11% (mean: 5%) in tension and from -3% to 23% (mean: 4%) in compression, while capturing the unloading and reloading behaviour. Overall, the *Steel02* models provide a more accurate representation of cyclic behaviour, particularly in capturing geometric and nonlinear effects, with the average MAE values for stainless steel rebars being approximately 11% lower than those of the *Hysteretic* models (Tables B.4 and B.5). Consequently, *Steel02* is recommended for modelling rebars in continuum reinforced concrete components subjected to cyclic loading.

5.3. Regression models for uniaxial cyclic model parameters

Correlations were observed between the *Steel02* and *Hysteretic* cyclic model parameters and the rebar L/D slenderness ratio. Consequently, regression analysis was conducted to develop relationships between the calibrated parameters and the slenderness ratio. The statistical significance of the proposed relationships was evaluated using p -values, with only those satisfying the threshold ($p \leq 0.05$) considered significant. For parameters that did not exhibit a statistically significant relationship with L/D , a constant value, based on the mean fitted values for the examined L/D data, was proposed. The presented regression models may be used to predict the cyclic model parameters for rebars of the same material grade and diameter with different L/D ratios. For parameters for which relationships were proposed, the regression models predicted calibrated values with average absolute percentage errors ranging from 2% to 28% across parameters. The regression relationships for the calibrated *Steel02* and *Hysteretic* cyclic model parameters, derived from the truss and beam-column rebar models, are summarised in Tables 5, 6, 7 and 8, with all symbols defined previously. The corresponding regression plots are provided in Appendix C.

Table 5
Regression relationship for *Steel02* cyclic truss model parameters.

Rebar	b	R_0	a_1	a_3
EN 1.4301-CR	0.018	$\begin{cases} 11.72, L/D = 5 \\ -0.97 \frac{L}{D} + 23.10, L/D \geq 8 \end{cases}$	$-0.116 \log \frac{L}{D} + 0.179$	$-0.122 \log \frac{L}{D} + 0.205$
EN 1.4301-HR	0.019	$\begin{cases} 14.90, L/D = 5 \\ -1.07 \frac{L}{D} + 26.21, L/D \geq 8 \end{cases}$	$-0.112 \log \frac{L}{D} + 0.192$	$-0.106 \log \frac{L}{D} + 0.172$
EN 1.4482-HR	0.016	$\begin{cases} 14.39, L/D = 5 \\ -0.97 \frac{L}{D} + 23.62, L/D \geq 8 \end{cases}$	$-0.103 \log \frac{L}{D} + 0.166$	$-0.100 \log \frac{L}{D} + 0.157$
B500C 12 mm	$-0.0012 \frac{L}{D} + 0.023$	$\begin{cases} 16.70, L/D = 5 \\ -1.45 \frac{L}{D} + 29.88, L/D \geq 8 \end{cases}$	$-0.067 \log \frac{L}{D} + 0.086$	$-0.063 \log \frac{L}{D} + 0.081$
B500C 16 mm	$-0.0015 \frac{L}{D} + 0.026$	$\begin{cases} 18.75, L/D = 5 \\ -1.59 \frac{L}{D} + 32.15, L/D \geq 8 \end{cases}$	$-0.071 \log \frac{L}{D} + 0.089$	$-0.067 \log \frac{L}{D} + 0.078$

Table 6
Regression relationship for *Steel02* cyclic beam-column model parameters.

Rebar	b	R_0	a_1	a_3
EN 1.4301-CR	0.0014	10.89	0.0120	0.0237
EN 1.4301-HR	0.0008	13.50	0.0420	0.0278
EN 1.4482-HR	0.0003	11.83	0.0320	0.0268
B500C 12 mm	0.0014	$-0.52L/D + 17.91$	0.0008	0.0040
B500C 16 mm	0.0011	$-0.48L/D + 17.88$	0.0064	0.0017

Table 7
Regression relationship for *Hysteretic* cyclic truss model parameters.

Rebar	PinchX	PinchY	Damage1	Damage2	β_{μ}
EN 1.4301-CR	0.43	-0.054L/D + 1.08	0	0.57 log L/D-0.90	0.34
EN 1.4301-HR	0.42	-0.076L/D + 1.34	0	0.53 log L/D-0.81	0.27
EN 1.4482-HR	0.058L/D-0.02	-0.023L/D + 0.91	0	0.77 log L/D-1.26	0.26
B500C 12 mm	0.060L/D-0.17	-0.026L/D + 0.74	0	0.22 log L/D-0.20	0.23
B500C 16 mm	0.049L/D-0.05	-0.032L/D + 0.80	0	0.22 log L/D-0.18	0.21

Table 8
Regression relationship for *Hysteretic* cyclic beam-column model parameters.

Rebar	PinchX	PinchY	Damage1	Damage2	β_{μ}
EN 1.4301-CR	0.33	0.80	0	0.003L/D-0.02	0.30
EN 1.4301-HR	0.23	0.97	0	0.004L/D-0.02	0.23
EN 1.4482-HR	0.26	0.95	0	0.005L/D-0.03	0.24
B500C 12 mm	0.11	0.60	0	0.004L/D-0.02	0.20
B500C 16 mm	0.12	0.62	0	0.005L/D-0.02	0.18

6. Model validation

The proposed rebar modelling approaches were validated by simulating reinforced concrete column tests subjected to cyclic loading using both standard fibre-section beam-column models in OpenSees and continuum models in the Scientific Toolkit for OpenSees (STKO). The tests on reinforced concrete columns with austenitic stainless steel and carbon steel rebars reported in Moodley et al. [4] were modelled. The columns had a height of 2 m, consisting of a 1.6 m long 400 mm diameter circular section and a 0.4 m long 500 mm × 500 mm square section at the top to facilitate cyclic loading. Each column was cast into a rigid foundation block. The sections were reinforced with nine 16 mm diameter longitudinal rebars and 8 mm diameter transverse rebars spaced at 80 mm, with a clear cover of 30 mm. Further details of the specimens and loading protocol are provided in Moodley et al. [4].

6.1. Column model development

6.1.1. Fibre-based column models

The columns were modelled using the nonlinear force-based distributed plasticity beam-column element *forceBeamColumn* with fibre sections assigned at integration points to represent reinforcing steel, unconfined cover concrete and confined core concrete. A Gauss-Lobatto scheme with four integration points, including one at the base, was adopted [33]. The fibre mesh comprised 20 fibres in both radial and circumferential directions for the core and one radial by 20 circumferential fibres for the cover, consistent with [34]. The specimen geometry and reinforcement configuration from the tests were modelled, and the boundary conditions were defined to replicate the experimental setup, in which all degrees of freedom at the base were restrained and those at the loaded end were left free, as shown in Fig. 15. *Concrete02* and *Concrete04* material models were used to define the unconfined and confined concrete behaviours, respectively, with parameters listed in Table 9, where f_c is the maximum compressive strength, ϵ_c is the strain at the maximum compressive strength, ϵ_{cu} is the strain at crushing strength, and f_t is the tensile strength. The compressive strength of the unconfined concrete was taken as the measured 28-day cylinder strength, while that of the confined concrete was obtained from the Mander et al. [35] model. Based on the findings presented in Section 5.1, the reinforcing bars in the fibre-based column models were represented using the multi-linear *Hysteretic* material model, which was considered more suitable for capturing cyclic behaviour across the examined slenderness range. The calibration methodology described in Section 4.2 was applied to tensile, compressive and cyclic test data for $L/D = 5$ rebars used in the stainless steel columns to derive the *Hysteretic* model parameters (Table 10). For the carbon steel columns, B500C 16 mm rebars, consistent with those tested in Section 2, were used, with the calibrated parameters applied directly (Table 10). The *Hysteretic* model also implicitly accounts for rebar damage due to low-cycle fatigue and inelastic buckling through the *Damage1* and *Damage2* parameters, thereby reflecting the observed failure mode of the carbon steel column [4].

6.1.2. Continuum column models

The continuum models were developed using the Scientific Toolkit for OpenSees (STKO) [26] and OpenSees [1]. The reinforcing bars were modelled using beam-column elements assembled into a rebar cage as shown in Fig. 16. For the longitudinal rebars at the base, above the foundation block, six beam-column elements were defined between the first pair of stirrups, incorporating a half-sine initial imperfection with an amplitude of $L/1000$ to account for geometric nonlinearities, consistent with the beam-column rebar modelling methodology described in Section 4.1. The concrete was modelled using 3D four-node tetrahedral elements with a mesh size of 25 mm. The rebar nodes were constrained to the surrounding concrete nodes using the *ASDEmbeddedNodeElement* command. Boundary conditions were applied by fully restraining all degrees of freedom along the central 600 mm of the foundation block, while at the column top, all degrees of freedom except the vertical displacement were restrained. The concrete was modelled using the *ASDConcrete3D* material model, calibrated against the unconfined *Concrete02* model based on parameters reported in Table 9. The elastic modulus E_c was set to 40,000 MPa and Poisson's ratio ν to 0.15. The fracture energies for the compression and tension softening

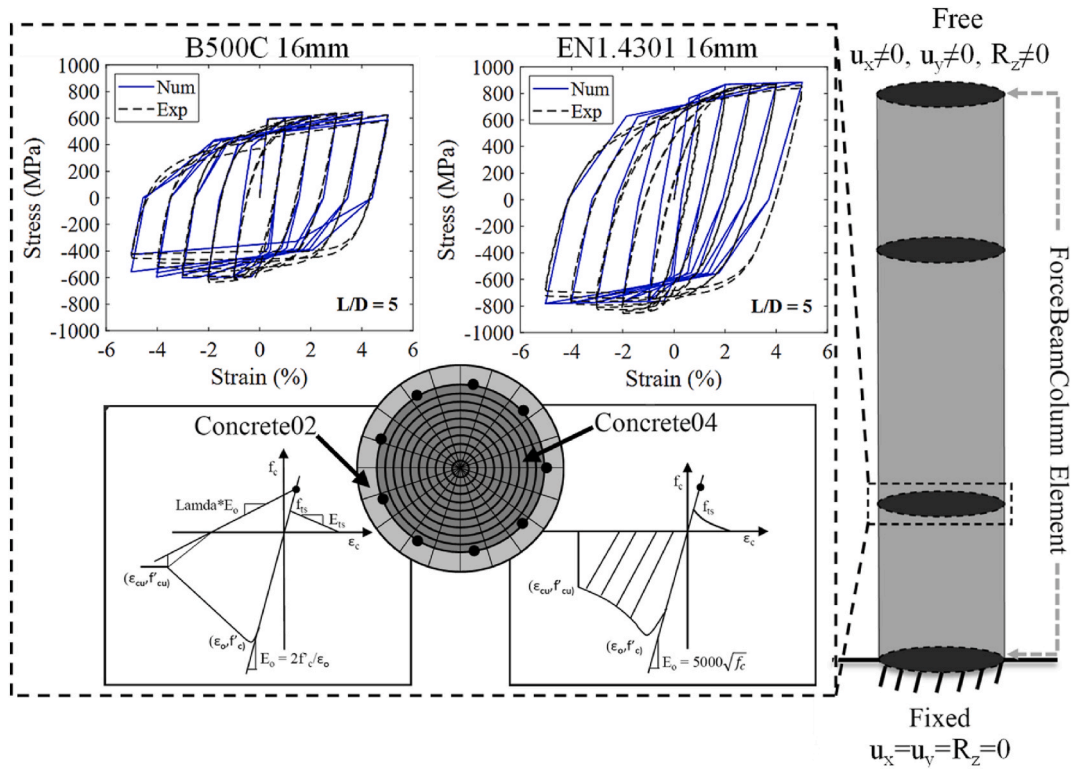


Fig. 15. Fibre-section column model validation [4].

Table 9
Unconfined Concrete02 and confined Concrete04 material model parameters.

Column	Concrete	f_c (MPa)	ϵ_c (%)	ϵ_{cu} (%)	f_t (MPa)
Carbon steel column	Unconfined	60.3	2.6	10.0	4.4
	Confined	70.9	4.9	22.0	4.4
Stainless steel column	Unconfined	52.1	2.5	10.0	4.1
	Confined	66.9	5.9	33.5	4.1

branches were taken as 0.27 N/mm and 0.05 N/mm, respectively, with all other parameters kept at their default values. As discussed in Section 5.2, the Steel02 model was used to represent the rebars in the continuum column analyses. The calibration methodology described in Section 4.2 was applied to the cyclic test data for $L/D = 5$ rebars used in the stainless steel columns to derive the Steel02 model parameters, while for the B500C 16 mm carbon steel rebars, the previously calibrated parameters were directly adopted, as

Table 10
Hysteretic material model parameters for steel rebars.

Model parameter	Carbon steel	Stainless steel
σ_{1p} (MPa)	594	764
ϵ_{1p} (%)	0.30	0.62
σ_{2p} (MPa)	668	868
ϵ_{2p} (%)	5.50	2.01
σ_{3p} (MPa)	682	952
ϵ_{3p} (%)	8.67	17.60
σ_{1n} (MPa)	594	764
ϵ_{1n} (%)	0.30	0.62
σ_{2n} (MPa)	615	797
ϵ_{2n} (%)	8.20	9.24
σ_{3n} (MPa)	343	566
ϵ_{3n} (%)	15.00	15.00
PinchX	0.14	0.26
PinchY	0.64	0.71
Damage1	0	0
Damage2	0.13	0
β_{mu}	0.23	0.30

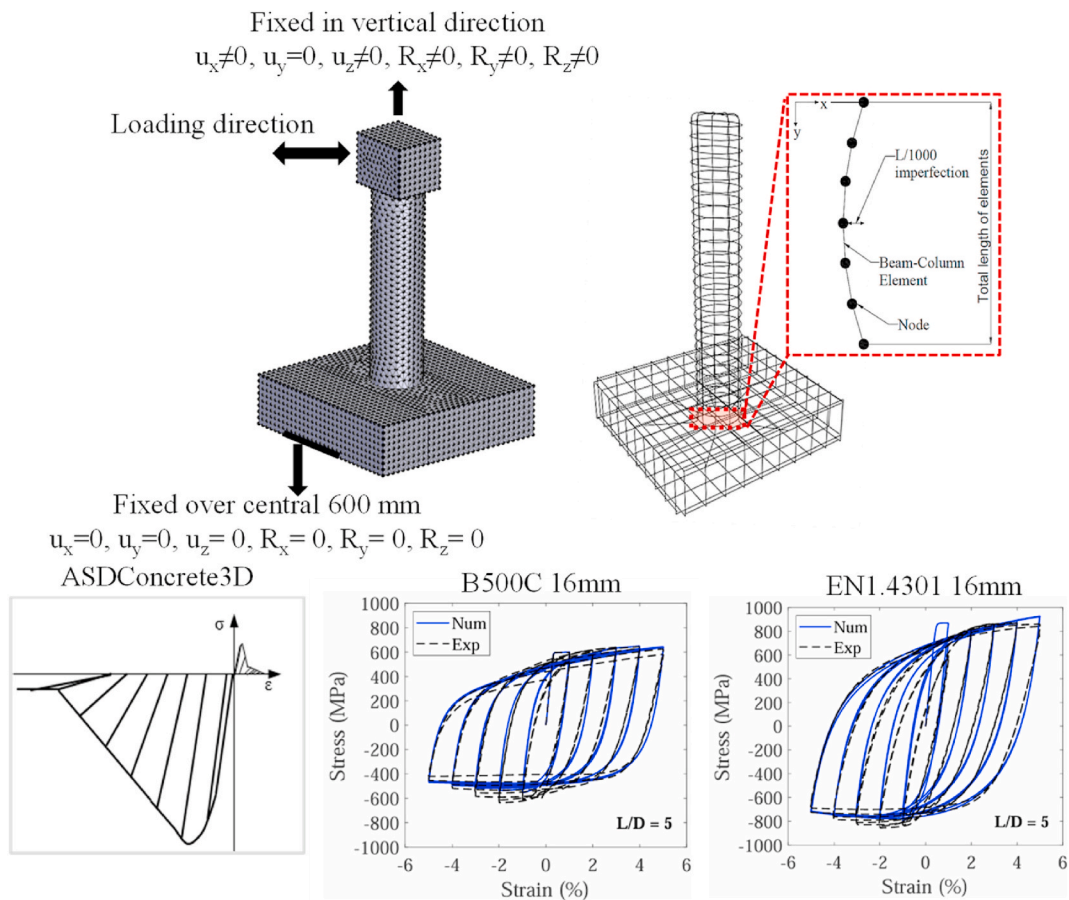


Fig. 16. Continuum STKO column model validation.

Table 11
Rebar *Steel02* cyclic model parameters continuum column models.

Model parameter	Carbon steel	Stainless steel
f_y (MPa)	594	869
E (MPa)	195500	192000
B	0.00463	0.00004
R_0	16.11	12.67
cR_1	0.925	0.925
cR_2	0.15	0.15
a_1	0.000	0.043
a_2	1.000	1.000
a_3	0.008	0.037
a_4	1.000	1.000

presented in Table 11. Since *Steel02* does not account for damage, the *Fatigue* wrapper was applied to incorporate low-cycle fatigue in the carbon steel columns, using Coffin-Manson strain-life parameters from Moodley, Afshan & De Risi [8].

6.2. Column model results

The numerical and experimental force-displacement responses for the fibre-based and continuum column models are shown in Figs. 17 and 18, respectively. In both cases, the simulations replicated the overall cyclic lateral response trends observed experimentally. For the fibre-based models, the responses agreed well with the experimental data but did not fully capture the pinching behaviour during reloading, particularly in the stainless steel column. For the continuum models, the agreement was similarly good, with the carbon steel column model also capturing the sudden strength loss beyond 3% drift in the positive loading direction. Nonetheless, as with the fibre-based simulations, the continuum models did not reproduce the full extent of pinching and tended to overestimate stiffness and strength at drift levels below 2%. However, these discrepancies are attributed to the assumptions of a perfect bond, which neglects strain penetration and reinforcement-concrete slip, as well as the idealised boundary conditions imposed in the numerical models. In the fibre-

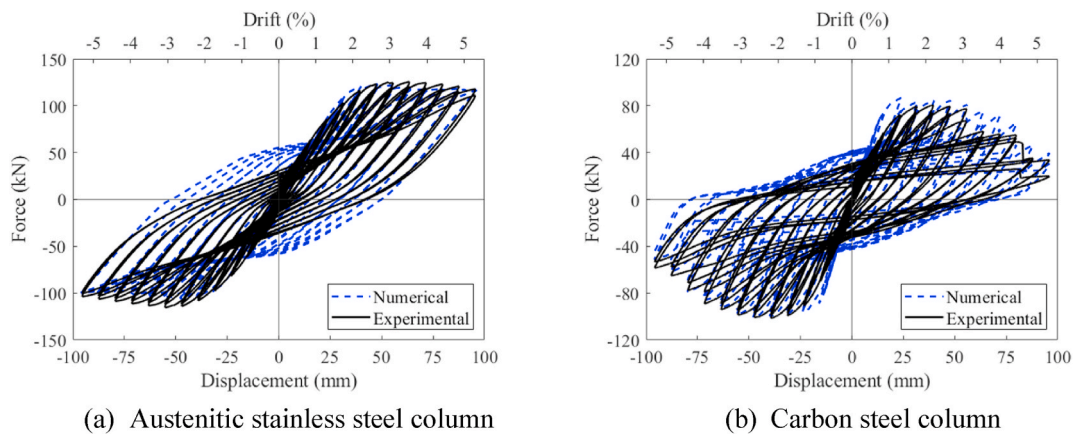


Fig. 17. Comparison of lateral force-drift responses from test and numerical fibre-based column models.

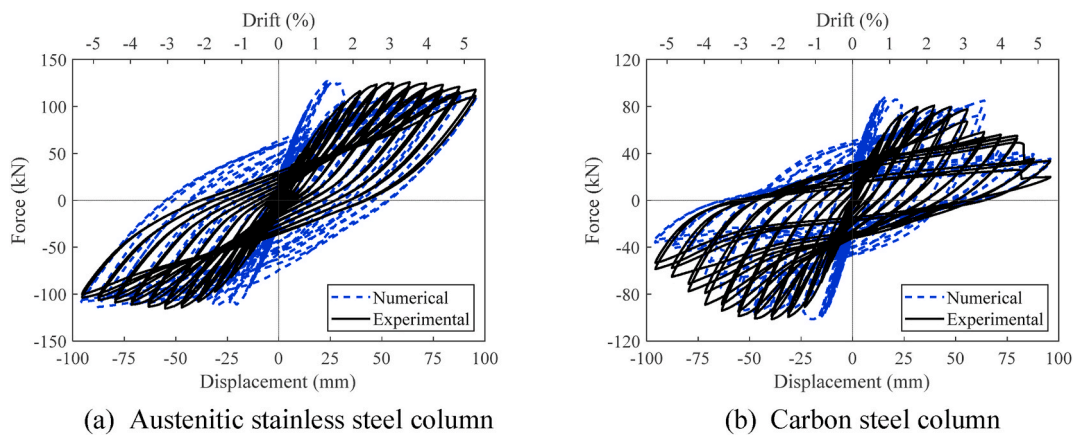


Fig. 18. Comparison of lateral force-drift responses from test and numerical continuum column models.

based models, the stainless steel column matched the experimental peak force in the positive direction but slightly underestimated it in the negative direction, while the carbon steel column over-predicted in the positive direction and agreed well in the negative direction. The continuum stainless steel model achieved closer agreement in both directions, whereas the carbon steel model showed the same trend as in the fibre-based model. However, for both materials, the continuum models reached peak forces at lower drift values than observed experimentally, reflecting the influence of perfect bond and idealised boundary conditions. The evolution of hysteretic energy dissipation per unit volume from the fibre-based and continuum column models is compared with the experimental results in Fig. 19a and b. In the fibre-based models, energy dissipation is initially underestimated ($<1\%$ drift for carbon steel and $<3\%$ for stainless steel) but is overestimated at higher drifts due to the inability to reproduce the pinching behaviour observed experimentally. The continuum model shows closer agreement at low drifts ($<1\%$) but similarly overestimates energy dissipation beyond this level, reflecting both the limited capture of pinching effects and the overestimation of stiffness and peak forces at drifts below 2% .

The validation of the fibre-based and continuum column models has shown that the calibration procedure for rebar material models developed in this study provides a systematic and repeatable methodology, capable of capturing the overall experimental trends in the lateral force–displacement response of stainless and carbon steel reinforced concrete columns. Furthermore, for the carbon steel column, the continuum model captured the sudden drop in force in the positive loading direction, a feature not reproduced by the fibre-based models. However, although the models reproduced the global response, they did not fully replicate the pinching behaviour or the evolution of energy dissipation observed in the tests. This limitation is attributed to the assumed perfect-bond conditions, which neglect strain penetration and bond–slip, both of which are known to influence unloading–reloading stiffness and pinching at the member level. It may also reflect the idealised boundary conditions and the simplified assumption that buckling can occur only over the stirrup spacing. This neglects the influence of transverse reinforcement stiffness on the effective buckling length of longitudinal reinforcement, which may exceed the assumed value [15]. Future work should aim to improve the predicted force–displacement response by: (i) incorporating strain penetration and bond–slip (e.g., in fibre-based models using a zero-length element at the column base with a calibrated strain-penetration model, and in continuum models by introducing a bond–slip law for steel–concrete interaction calibrated for carbon and stainless steel rebars), requiring reliable bond–slip test data for the investigated rebars, particularly the stainless steel grades, to support calibration. (ii) Exploring less idealised boundary conditions (e.g., relaxing the fully fixed assumption in the loading direction); and (iii) investigating buckling-length models such as that proposed in [15].

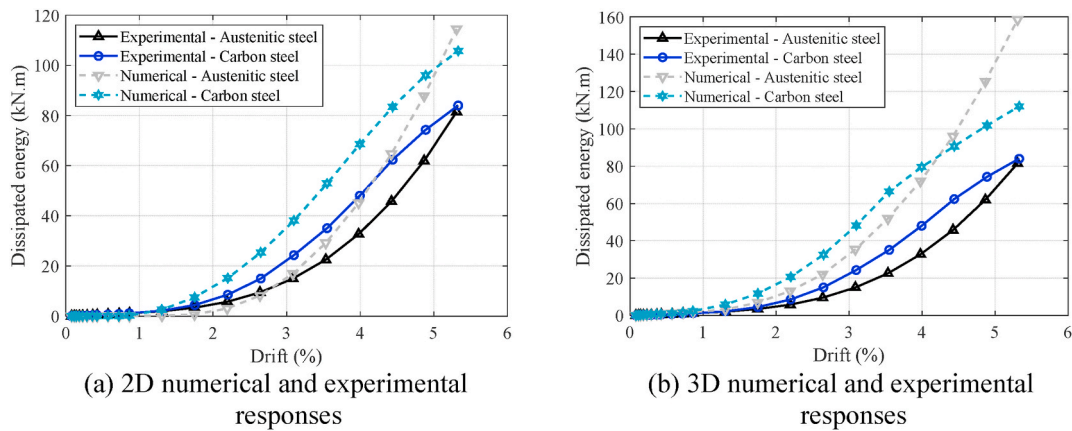


Fig. 19. Comparisons of the experimental and numerical hysteretic dissipated energy per unit volume evolutions of columns: (a) fibre-based models, (b) continuum models.

7. Conclusions

This study presented a systematic methodology for calibrating OpenSees uniaxial material models to accurately simulate the cyclic stress-strain behaviour of stainless steel rebars. New monotonic tension and compression and cyclic experimental tests were conducted on hot-rolled and cold-rolled austenitic EN 1.4301, hot-rolled lean duplex EN 1.4482, and B500C carbon steel rebars. The investigation focused on the *Steel02* and *Hysteretic* uniaxial material models, utilising the Particle Swarm Optimisation (PSO) technique to calibrate their parameters based on both truss and beam-column rebar models. Truss-based calibration ensures accurate representation of rebars in fibre-section models. In contrast, the calibration of beam-column rebar models is critical for the precise simulation of steel rebar within continuum reinforced concrete structural components. The main conclusions were as follows.

- For truss rebar models, *Hysteretic* models more reliably captured the experimental cyclic trends across a broader range of slenderness than *Steel02* models. For example, the *Hysteretic* models per-model mean percentage errors in peak stress (averaged over all cycles) were -7% to 11% in tension (mean: 1%) and -23% to 10% in compression (mean: -7%), compared with *Steel02* models at -49% to -5% in tension (mean: -25%) and 5% to 38% in compression (mean: 24%).
- For beam-column rebar models, where geometric nonlinearities are explicitly accounted for, the *Steel02* model more accurately captured the observed responses, including unloading and reloading stiffnesses and pinching in compression, compared to the *Hysteretic* model. The per-modal mean percentage errors in peak stress (averaged over all cycles) were -7% to 5% in tension (mean: -0.1%) and -11% to 14% in compression (mean: 3%) for *Steel02* models, versus -5% to 11% in tension (mean: 0.5%) and -5% to 23% in compression (mean: 4%) for *Hysteretic* models.
- Regression models were developed to relate the calibrated parameters of the cyclic model to the rebar slenderness ratio (L/D). For parameters for which relationships were proposed, the regression models predicted calibrated values, with average absolute percentage errors ranging from 2% to 28% across parameters. These models provide a practical tool for predicting cyclic model parameters for rebars of the same material grade and diameter but with different L/D ratios, thereby enhancing the applicability of the calibrated models for future simulations of carbon and stainless steel reinforced concrete components.
- Numerical modelling simulations of stainless and carbon steel reinforced concrete circular columns under cyclic loading verified that the proposed rebar calibration procedure provides a consistent and reliable approach for simulating the cyclic response of stainless and carbon steel reinforced concrete columns.
- While the models captured the overall lateral force–displacement trends, further refinement incorporating bond–slip and strain penetration, adopting less idealised boundary conditions, and assessing the assumed reinforcement buckling length to improve representation of pinching and energy dissipation behaviour.

CRedit authorship contribution statement

H. Moodley: Writing – original draft, Methodology, Investigation, Formal analysis, Conceptualization. **R. De Risi:** Writing – review & editing, Methodology, Conceptualization. **S. Afshan:** Writing – review & editing, Supervision, Methodology, Conceptualization.

Declaration of competing interest

As the corresponding author of the above-named manuscript, and on behalf of my co-authors, I wish to confirm that there are no known conflicts of interest associated with this publication and there has been no significant financial support for this work that could have influenced its outcome.

Appendix A. Measured stress-strain responses for carbon steel rebar

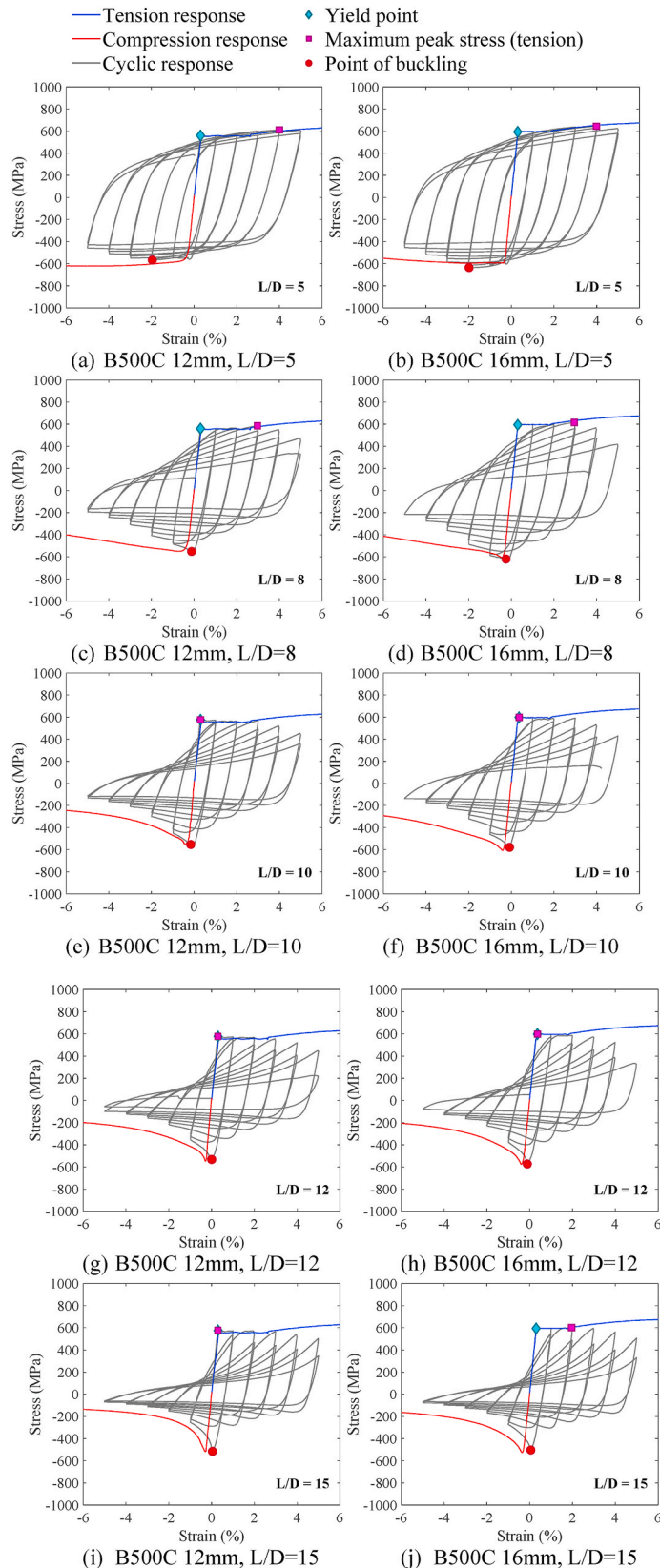


Fig. A.1. Cyclic stress-strain responses of carbon steel rebars

Appendix B. Calibrated model parameters

Table B.1
Calibrated parameters and MAE for *Steel02* cyclic truss model.

Rebar	L/D	f_y (MPa)	b	R_0	a_1	a_3	MAE (MPa)
EN 1.4301-CR	5	825	0.010	11.72	0.012	0.026	71.3
	8	825	0.027	15.35	-0.082	-0.071	96.6
	10	825	0.021	13.55	-0.101	-0.089	92.5
	12	825	0.019	11.07	-0.115	-0.101	98.3
	15	825	0.012	8.67	-0.110	-0.107	94.1
EN 1.4301-HR	5	713	0.016	14.90	0.025	0.016	60.9
	8	713	0.027	17.38	-0.054	-0.065	79.6
	10	713	0.020	15.82	-0.081	-0.083	74.9
	12	713	0.019	13.27	-0.086	-0.092	85.4
	15	713	0.011	10.02	-0.095	-0.100	83.0
EN 1.4482-HR	5	739	0.008	14.39	0.009	0.008	52.7
	8	739	0.030	15.91	-0.056	-0.066	84.3
	10	739	0.023	14.41	-0.081	-0.086	82.6
	12	739	0.010	11.29	-0.094	-0.093	81.5
	15	739	0.010	9.45	-0.100	-0.100	81.9
B500C 12 mm	5	560	0.016	16.70	-0.012	-0.012	48.3
	8	560	0.014	18.86	-0.065	-0.063	59.6
	10	560	0.012	14.87	-0.075	-0.072	62.0
	12	560	0.008	11.88	-0.084	-0.078	59.0
	15	560	0.004	8.57	-0.084	-0.080	61.5
B500C 16 mm	5	594	0.016	18.75	-0.018	-0.019	53.9
	8	594	0.018	19.78	-0.062	-0.077	73.2
	10	594	0.011	15.92	-0.087	-0.084	64.3
	12	594	0.007	12.72	-0.094	-0.095	62.8
	15	594	0.004	8.55	-0.090	-0.091	63.6

Table B.2
Calibrated ϵ (%) and σ (MPa) parameters, and MAE (MPa), for the tensile and compressive backbones of the *Hysteretic* cyclic truss model.

Rebar	L/D	Tensile backbone			MAE	Compression backbone			MAE
		$\epsilon_{1p}, \sigma_{1p}$	$\epsilon_{2p}, \sigma_{2p}$	$\epsilon_{3p}, \sigma_{3p}$		$\epsilon_{1n}, \sigma_{1n}$	$\epsilon_{2n}, \sigma_{2n}$	$\epsilon_{3n}, \sigma_{3n}$	
EN 1.4301-CR	5	0.33,677	1.58,812	21.75,872	12.3	0.33,677	8.19,741	15.00,469	124.3
	8					0.33,677	0.76,687	14.55,135	69.1
	10					0.33,677	2.90,532	12.81,135	63.7
	12					0.33,677	2.73,471	11.11,135	53.8
	15					0.33,677	2.60,374	8.57,135	40.8
EN 1.4301-HR	5	0.28,562	4.42,745	29.5819	20.9	0.28,562	7.99,656	15.00,376	149.7
	8					0.28,562	3.28,530	13.72,112	133.1
	10					0.28,562	2.18,442	10.41,112	82.8
	12					0.28,562	2.12,397	9.23,112	51.0
	15					0.28,562	2.10,327	7.46,112	39.5
EN 1.4482-HR	5	0.29,579	2.49,730	36.2827	13.6	0.29,579	7.93,676	15.00,393	152.2
	8					0.29,579	2.32,611	14.71,116	77.9
	10					0.29,579	2.59,477	11.62,116	79.1
	12					0.29,579	2.29,435	10.28,116	53.2
	15					0.29,579	2.00,358	8.26,116	32.6
B500C 12 mm	5	0.28,560	6.80,644	11.4657	4.7	0.28,560	7.79,589	15.00,300	82.1
	8					0.28,560	3.21,476	12.32,112	80.3
	10					0.28,560	2.00,418	9.65,112	50.1
	12					0.28,560	2.00,374	8.55,112	36.9
	15					0.28,560	1.99,308	6.90,112	34.9
B500C 16 mm	5	0.30,594	5.50,812	21.75,872	4.9	0.30,594	8.20,615	15.00,343	41.9
	8					0.30,594	3.09,499	12.60,119	68.2
	10					0.30,594	2.17,438	10.16,119	41.4
	12					0.30,594	2.17,390	8.96,119	38.3
	15					0.30,594	2.16,318	7.14,119	26.4

Table B.3
Calibrated parameters and MAE for *Hysteretic* cyclic truss model.

Rebar	L/D	PinchX	PinchY	Damage1	Damage2	β_{mu}	MAE (MPa)
EN 1.4301-CR	5	0.29	0.79	0.000	0.000	0.40	69.5
	8	0.31	0.53	0.000	0.242	0.31	78.6
	10	0.51	0.70	0.000	0.519	0.30	74.1
	12	0.52	0.50	0.000	0.570	0.30	75.0
	15	0.50	0.18	0.000	0.564	0.32	75.1
EN 1.4301-HR	5	0.24	1.00	0.000	0.120	0.36	90.3
	8	0.44	0.73	0.000	0.186	0.27	92.7
	10	0.50	0.55	0.000	0.288	0.19	98.2
	12	0.42	0.32	0.000	0.552	0.26	87.3
	15	0.51	0.28	0.000	0.679	0.25	71.1
EN 1.4482-HR	5	0.22	0.85	0.000	0.000	0.29	81.0
	8	0.43	0.65	0.000	0.291	0.30	82.7
	10	0.67	0.64	0.000	0.408	0.30	90.8
	12	0.64	0.64	0.000	0.928	0.25	82.6
	15	0.61	0.58	0.000	0.710	0.19	76.6
B500C 12 mm	5	0.15	0.67	0.000	0.135	0.28	36.8
	8	0.25	0.45	0.004	0.243	0.24	69.7
	10	0.44	0.47	0.000	0.343	0.22	67.4
	12	0.59	0.41	0.004	0.362	0.24	63.6
	15	0.70	0.38	0.000	0.308	0.19	57.4
B500C 16 mm	5	0.14	0.64	0.000	0.131	0.23	45.2
	8	0.37	0.51	0.000	0.339	0.21	84.5
	10	0.48	0.51	0.000	0.384	0.21	69.6
	12	0.60	0.42	0.000	0.368	0.20	66.0
	15	0.62	0.31	0.000	0.327	0.19	63.5

Table B.4
Calibrated parameters and MAE for *Steel02* cyclic beam-column model.

Rebar	L/D	f_y (MPa)	b	R_0	a_1	a_3	MAE (MPa)
EN 1.4301-CR	5	825	0.00326	11.53	0.040	0.049	63.9
	8	825	0.00069	11.40	0.010	0.026	61.0
	10	825	0.00213	10.74	0.000	0.014	60.5
	12	825	0.00074	10.39	0.000	0.012	45.1
	15	825	0.00000	10.40	0.010	0.017	36.6
EN 1.4301-HR	5	713	0.00304	13.85	0.050	0.047	47.4
	8	713	0.00073	13.72	0.040	0.031	34.8
	10	713	0.00000	13.84	0.030	0.016	26.9
	12	713	0.00014	13.04	0.050	0.027	27.3
	15	713	0.00004	13.05	0.040	0.020	19.8
EN 1.4482-HR	5	739	0.00136	12.65	0.040	0.043	49.6
	8	739	0.00000	11.51	0.050	0.039	45.3
	10	739	0.00001	11.71	0.040	0.026	36.8
	12	739	0.00019	11.97	0.020	0.017	30.2
	15	739	0.00015	11.30	0.010	0.010	20.0
B500C 12 mm	5	560	0.00539	15.77	0.000	0.011	36.0
	8	560	0.00110	13.21	0.000	0.003	38.8
	10	560	0.00002	12.80	0.001	0.003	27.9
	12	560	0.00001	11.55	0.000	0.002	29.4
	15	560	0.00042	10.45	0.003	0.000	18.9
B500C 16 mm	5	594	0.00463	16.11	0.000	0.008	41.0
	8	594	0.00050	13.57	0.020	0.000	43.6
	10	594	0.00003	12.41	0.007	0.001	29.7
	12	594	0.00009	11.99	0.002	0.000	29.4
	15	594	0.00052	11.13	0.003	0.000	18.7

Table B.5
Calibrated parameters and MAE for *Hysteretic* cyclic beam-column model.

Rebar	L/D	PinchX	PinchY	Damage1	Damage2	β_{μ}	MAE (MPa)
EN 1.4301-CR	5	0.38	0.97	0.000	0.000	0.39	91.5
	8	0.38	0.87	0.000	0.000	0.25	64.8
	10	0.32	0.73	0.001	0.017	0.30	48.5
	12	0.33	0.72	0.001	0.016	0.29	40.1
	15	0.24	0.71	0.001	0.033	0.29	25.0
EN 1.4301-HR	5	0.23	0.98	0.000	0.000	0.32	76.1
	8	0.25	0.99	0.000	0.006	0.26	43.0
	10	0.24	0.98	0.000	0.027	0.16	36.0
	12	0.25	0.98	0.000	0.022	0.23	37.7
	15	0.20	0.92	0.000	0.044	0.20	30.5
EN 1.4482-HR	5	0.26	0.97	0.000	0.000	0.25	81.5
	8	0.31	0.97	0.000	0.000	0.25	52.5
	10	0.28	0.94	0.000	0.025	0.26	36.4
	12	0.24	0.94	0.000	0.033	0.21	30.5
	15	0.22	0.94	0.000	0.047	0.18	23.6
B500C 12 mm	5	0.09	0.68	0.000	0.000	0.33	29.1
	8	0.13	0.63	0.000	0.017	0.14	24.4
	10	0.10	0.54	0.000	0.026	0.19	19.6
	12	0.14	0.62	0.000	0.037	0.16	17.9
	15	0.11	0.53	0.000	0.043	0.17	16.3
B500C 16 mm	5	0.09	0.69	0.000	0.000	0.24	32.3
	8	0.17	0.76	0.000	0.025	0.17	28.5
	10	0.10	0.54	0.000	0.041	0.19	19.4
	12	0.16	0.58	0.000	0.026	0.14	17.7
	15	0.10	0.53	0.000	0.053	0.17	12.2

Appendix C. Regression plots

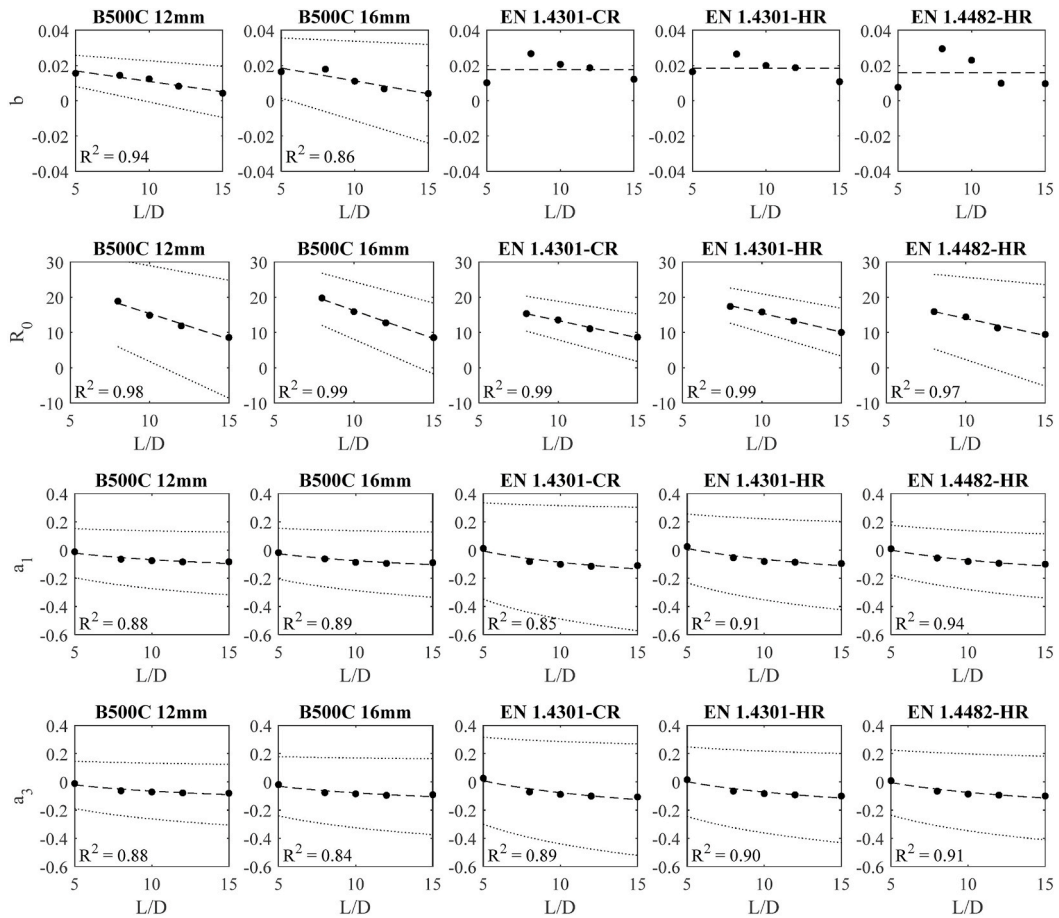


Fig. C.1. Regression analysis for truss *Steel02* cyclic model parameters with 95 % confidence intervals.

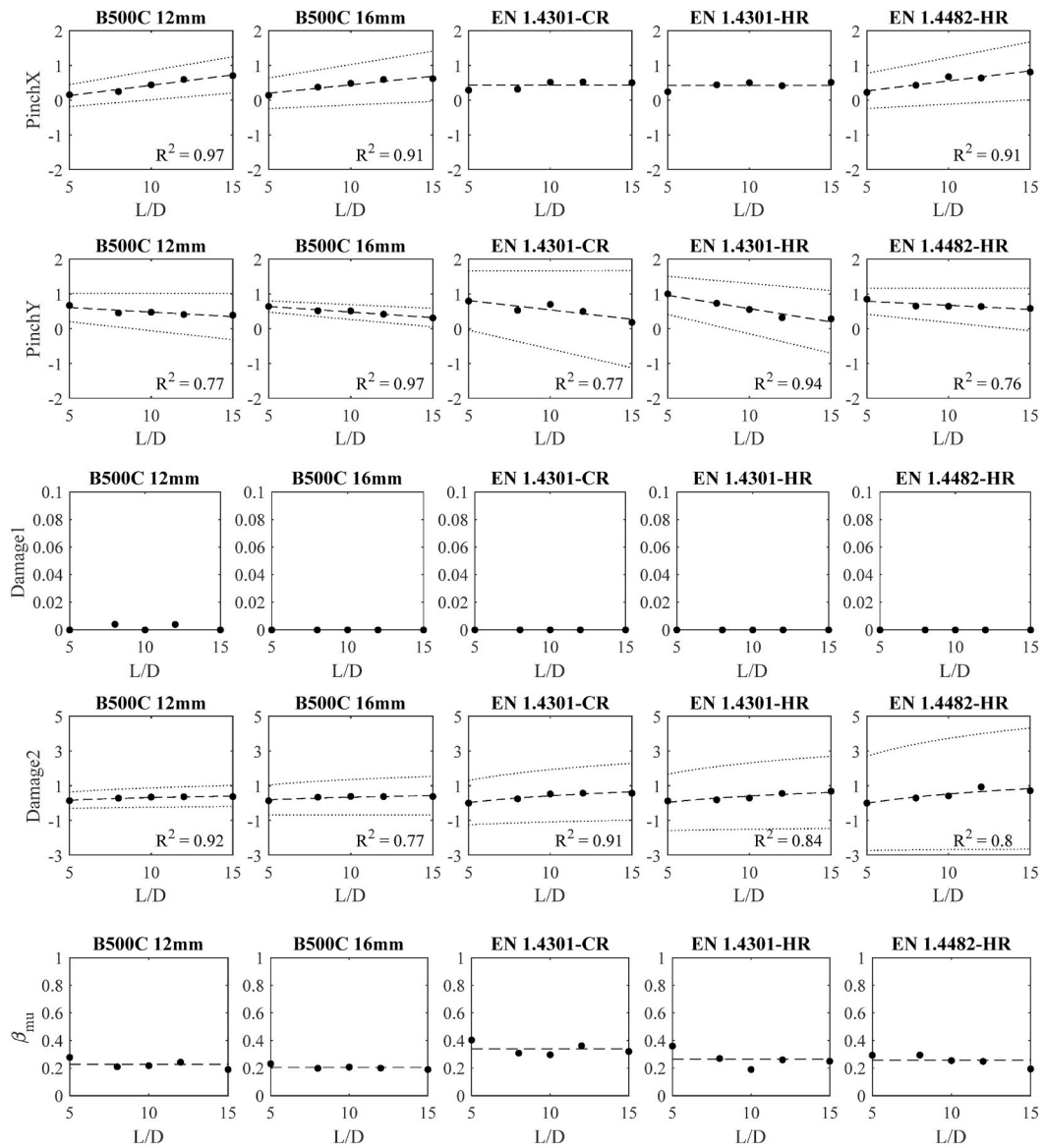


Fig. C.2. Regression analysis for truss *Hysteretic* cyclic model parameters with 95 % confidence intervals.

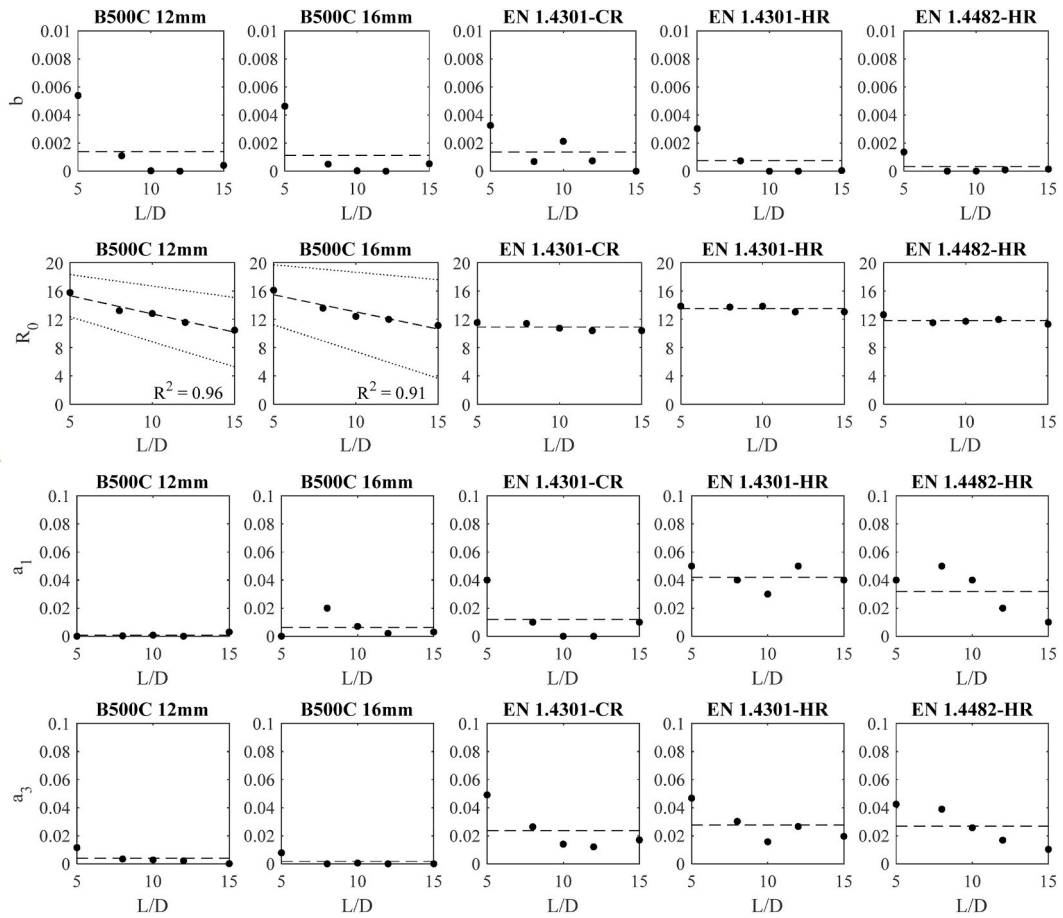


Fig. C.3. Regression analysis for beam-column *Steel02* cyclic model parameters with 95 % confidence intervals.

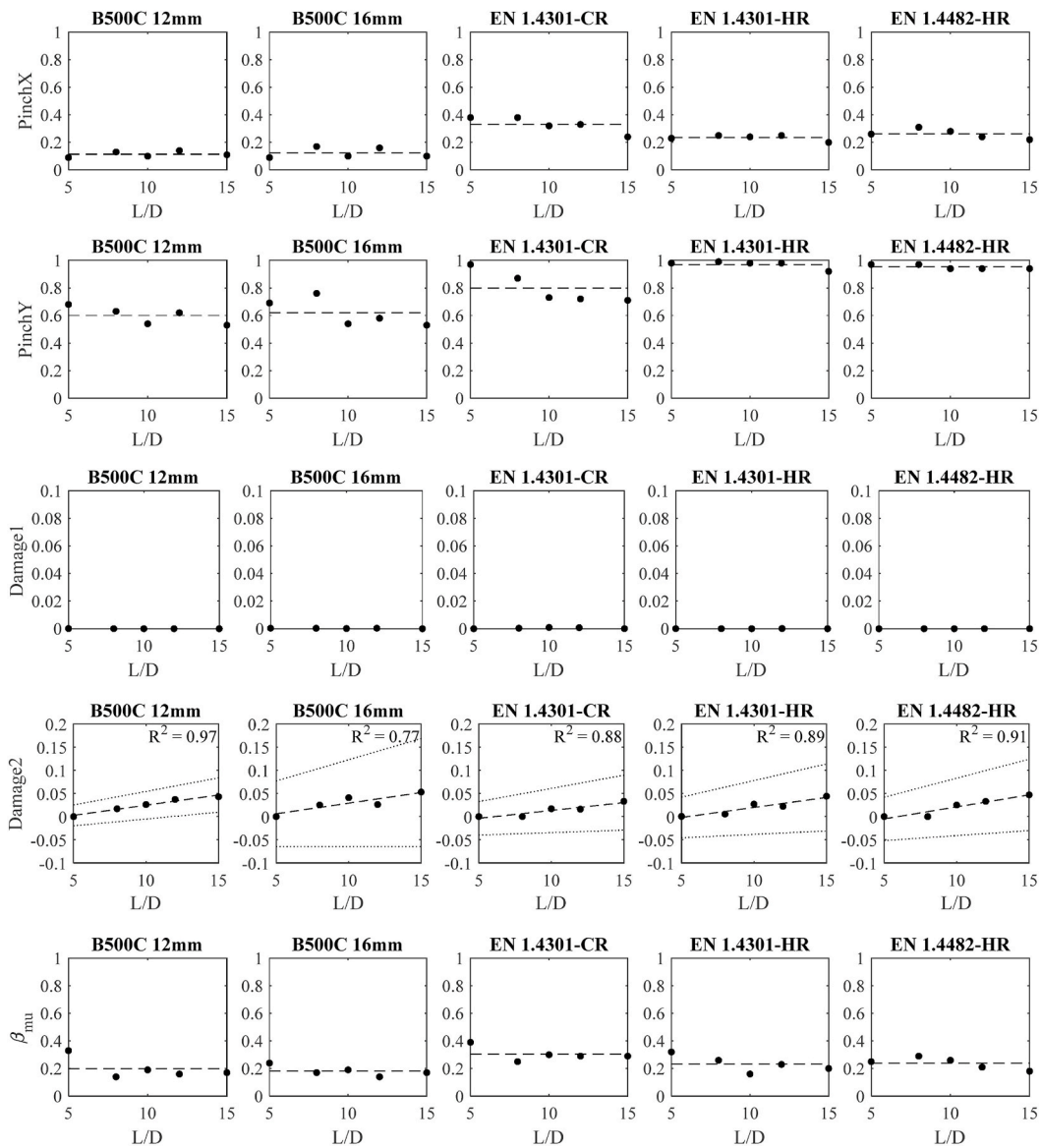


Fig. C.4. Regression analysis for beam-column *Hysteretic* cyclic model parameters with 95 % confidence intervals.

Data availability

Data will be made available on request.

References

- [1] S. Mazzoni, F. McKenna, M.H. Scott, G.L. Fenves, et al., *Opensees Command Language Manual*, Pacific Earthquake Engineering Research Center, University of California, 2007.
- [2] Seissoft, *SeismoStruct 2024 – a computer program for static and dynamic nonlinear analysis of framed structures* [Online]. Available: <https://seissoft.com/>, 2024.
- [3] Computers and Structures Inc, “SAP2000 Structural Analysis and Design Software,” 2024.
- [4] H. Moodley, S. Afshan, D. Crump, M.M. Kashani, Testing and numerical modelling of circular stainless steel reinforced concrete columns, *Eng. Struct.* 304 (2024) 117607.
- [5] J. Melo, S. Afshan, T. Rossetto, Y. Varum, A. Arède, Experimental and numerical investigation of the cyclic response of stainless steel reinforced concrete columns, *Eng. Struct.* 252 (2021).
- [6] J.Y. Fu, X. Ge, J.T. Li, Z.G. Sun, D.S. Wang, Seismic performance of concrete bridge piers reinforced by stainless steel bars: a quasi-static experimental study, *Engineering Structures* 266 (2022).

- [7] J. Limbert, S. Afshan, M.M. Kashani, A.F. Robinson, Compressive stress–strain behaviour of stainless steel reinforcing bars with the effect of inelastic buckling, *Eng. Struct.* 237 (2021).
- [8] H. Moodley, S. Afshan, R. De Risi, Low-cycle fatigue behaviour and strain-life model of stainless steel reinforcing bars, *Structures* 67 (2024) 106994.
- [9] H. Moodley, S. Afshan, S. Blainey, J. Preston, State-of-the-art review on the structural behaviour of stainless steel reinforced concrete elements, in: 11th International Conference on Bridge Maintenance, Safety and Management, 2022.
- [10] M. Rabi, R. Shamass, K.A. Cashell, Structural performance of stainless steel reinforced concrete members: a review, *Constr. Build. Mater.* 325 (2022) 126673 [Online]. Available: <https://www.sciencedirect.com/science/article/pii/S0950061822003646>.
- [11] J. Yuan, Z. Ou, Research progress and engineering applications of stainless steel-reinforced concrete structures, *Adv. Civ. Eng.* 2021 (2021) 9228493 [Online].
- [12] Q. Han, M. Hu, K. Xu, X. Du, Hysteretic behavior and modelling of ultra-high-strength steel bar including buckling, *Bull. Earthq. Eng.* 17 (2019) 5265–5289.
- [13] M.M. Kashani, L.N. Lowes, A.J. Crewe, N.A. Alexander, Phenomenological hysteretic model for corroded reinforcing bars including inelastic buckling and low-cycle fatigue degradation, *Comput. Struct.* 156 (2015) 58–71.
- [14] R. Carreño, K.H. Lotfizadeh, J.P. Conte, J.I. Restrepo, Material model parameters for the giuffrè-menegotto-pinto uniaxial steel stress-strain model, *J. Struct. Eng.* 146 (2) (2020) 04019205.
- [15] L. Di Sarno, F. Pugliese, R. De Risi, Non-linear finite element optimization for inelastic buckling modelling of smooth rebars, *Eng. Struct.* 240 (2021) 112378.
- [16] CEN, EN 10088-1: Stainless Steels– Part 1: List of Stainless Steels, European Committee for Standardization, Brussels, 2023.
- [17] G. Carmine, M. Giuseppe, C. Edoardo, Uncertainly analysis of flexural overstrength for capacity design of RC beams, *J. Struct. Eng.* 140 (7) (Jul. 2014) 04014037.
- [18] G.M. Verderame, P. Ricci, M. Esposito, F.C. Sansiviero, Le Caratteristiche Meccaniche Degli Acciai Impiegati Nelle Strutture in Ca Realizzate Dal 1950 Al 1980, XXVI Convegno Nazionale AICAP, 2011.
- [19] CEN, EN 1992-1-1 Eurocode 2, Design of Concrete Structures. Part 1-1: General Rules and Rules for Buildings, Bridges and Civil Engineering Structures, European Committee for Standardization, Brussels, 2023.
- [20] CEN, EN ISO 6892-1: Metallic materials, Tensile Testing. Method of Test at Room Temperature, European Committee for Standardization, Brussels, 2019.
- [21] R.P. Dhakal, K. Maekawa, Reinforcement stability and fracture of cover concrete in reinforced concrete members, *J. Struct. Eng.* 128 (10) (2002) 1253–1262.
- [22] J.-Y. Tinevez, et al., TrackMate: an open and extensible platform for single-particle tracking, *Methods* 115 (2017) 80–90.
- [23] C.A. Schneider, W.S. Rasband, K.W. Eliceiri, NIH image to ImageJ: 25 years of image analysis, *Nat. Methods* 9 (7) (2012) 671–675.
- [24] M.M. Kashani, A.J. Crewe, N.A. Alexander, Nonlinear stress–strain behaviour of corrosion-damaged reinforcing bars including inelastic buckling, *Eng. Struct.* 48 (2013) 417–429.
- [25] F. Taucer, E. Spacone, F. Filippou, A Fiber beam-column Element for Seismic Response Analysis of Reinforced Concrete Structures, vol. 91, 1991. Berkeley.
- [26] M. Petracca, F. Candeloro, G. Camata, STKO User Manual, Asdea Software Technology, Pescara, 2021.
- [27] M. Menegotto, P.E. Pinto, Method of analysis of cyclically loaded RC plane frames including changes in geometry and nonelastic behaviour of elements under normal force and bending, in: Preliminary Report IABSE, 1973, pp. 15–22.
- [28] M.H. Scott, Hysteretic pinching parameters, Portwood Digital (2025) [Online]. Available: <https://portwooddigital.com/2020/12/27/hysteretic-pinching-parameters/>, 7-3.
- [29] M.H. Scott, Hysteretic damage parameters, Portwood Digital (2025) [Online]. Available: <https://portwooddigital.com/2022/04/17/hysteretic-damage-parameters/>, 7-3.
- [30] M. Bosco, A. Floridaia, D. Panarelli, P.P. Rossi, A new uniaxial material model for the simulation of lateral buckling of steel rebars, *Eng. Struct.* 323 (2025) 119293.
- [31] R.P. Dhakal, K. Maekawa, Modeling for postyield buckling of reinforcement, *J. Struct. Eng.* 128 (9) (2002) 1139–1147.
- [32] MathWorks, “MATLAB Global Optimization Toolbox User’s Guide R2024A:2024,” 2024.
- [33] K. Du, J. Sun, W. Xu, Evaluation of section and fiber integration points in fiber model, in: 15th World Conference on Earthquake Engineering, Curran Associates, Inc, 2012, pp. 9789–9795.
- [34] M.P. Berry, M.O. Eberhard, Performance Modeling Strategies for Modern Reinforced Concrete Bridge, University of California, Berkeley, 2008.
- [35] J.B. Mander, M.J.N. Priestley, R. Park, Theoretical stress-strain model for confined concrete, *J. Struct. Eng.* 114 (8) (1988) 1804–1826.